Università degli Studi di Bologna

Facoltà di Chimica Industriale

Corso di Laurea Magistrale in Chimica Industriale
Classe LM - 71 - Scienze e Tecnologie della Chimica Industriale

Dipartimento di Chimica Fisica e Inorganica

Atomistic simulations of bulk and free standing film smectics

Tesi di Laurea Magistrale

Presentata da:
Mattia Felice Palermo

Relatore:
Prof. Claudio Zannoni

Correlatori:
Dr. Luca Muccioli
Dr. Antonio Pizzirusso

Anno Accademico 2010–2011

II Sessione

Sommario

In questa tesi viene descritto lo studio delle fasi liquido-cristalline del 4-n-ottil - 4′-cianobifenile eseguito tramite simulazioni al calcolatore molecular dynamics, sia per campioni bulk che per film smectici sottili. Impiegando un campo di forze “molecular mechanics” precedentemente usato con successo per studiare sistemi composti da 250 molecole della serie degli n-cianobifenili (nCB, con n pari a 4-8 atomi di carbonio nella catena alifatica), si è simulato il comportamento di un sistema bulk di 750 molecole e di un film smectico di 1500 molecole. Nel primo caso, sottoponendo il campione a un graduale raffreddamento, si è osservata la formazione spontanea di fasi ordinate quali quella nematica e quella smectica. Nel secondo caso, invece, si è studiata l’influenza dell’interfaccia con il vuoto sull’ordine posizionale e orientazionale di film sottili di diverso spessore e temperatura. Si sono confrontate le proprietà di entrambi i sistemi simulati con i dati sperimentali disponibili in letteratura, confermando la bontà del modello nel riprodurre fedelmente le caratteristiche dei campioni reali.

Contents

List of Figures

List of Tables

Chapter 1

Liquid Crystals

1.1 History of liquid crystals

The discovery of liquid crystals (LC) dates back to 1888 when Professor Friedrich Reinitzer, an Austrian chemist and botanist working at the Institute of Plant Physiology of the University of Prague, observed a strange phenomenon. While trying to determine the melting point of cholesteryl benzoate in order to assess its purity, he was surprised to observe that such sustance seemed to have two melting points. The solid crystal melted first into a cloudy liquid at 145.5 °C, a state that persisted untill 178.5 °C, at which cloudiness suddenly disappeared leaving a transparent liquid. Even though Reinitzer hypothesized this was just an effect of impurities, further purifications did not change the behaviour of the liquid.

In order to explain such discovery, Reinitzer asked for help to Otto Lehmann, a German physicist expert in the field of crystal optics. Lehmann proposed that the cloudy state of the liquid was indeed a new state of the matter which shared some properties of both solids and liquids. In particular, he found that in contrast with common liquids, for which properties are isotropic, LCs align to each other after the application of a relatively weak field and thus their properties strongly depend on the direction in which they are measured, even if the substance is fluid. In 1889 he published the paper “Über fliessende Krystalle” (On flowing crystals), later coining the term “liquid crys-

tal", which emphasized the peculiar order of this phase. The existence of different phases other than the regular ones was not accepted with ease by the scientific community, as some scientists deprecated the newly discovered state of matter as just a mixture of solid and liquid components. In 1922, Friedel published his famous two-hundred page review in the Annales de Physique, setting out most of the basic classification of liquid crystals compounds into several categories: nematics, smectics and cholesteric. He also shed some light on the orienting effect of electric fields and on the presence of defects in liquid crystals. Between 1922 and 1939, Carl W. Oseen of the swedish University of Uppsala and Hans Zöcher of the University of Prague developed a macroscopic mathematical model for the study of liquid crystal order, introducing the formulation of the orientational order parameter.

The interest in the liquid crystal field slowly lapsed after the mid 30's due to the lack of technical applications and the belief that all significant problems in this area had been fully investigated. In 1936 a British patent for the first practical application of LC, "The Liquid Crystal Light Valve", was awarded to the Marconi Wireless Telegraph company, but nothing further came of this.

Only in the 1960s, some important studies and applications drawn new attention to LCs. From a theoretical point of view, a big leap in the knowledge of the soft matter physics was made by the French scientist Pierre-Gilles de Gennes, whose studies were awarded with the Nobel Prize in Physics later in 1991 and whose work "The Physics of Liquid Crystals" has become a classical textbook nowadays. In the same decade, a great breakthrough regarding technical applications of liquid crystals was made by George Heilmeier, who presented the first liquid crystal display in 1968 based on what he called the dynamic scattering mode (DSM). Application of a voltage to a DSM display switches the initially clear transparent liquid crystal layer into a milky turbid state. This type of display required a considerable current flow in order to operate and generated an excessive amount of heat. Still in 1968, the first room-temperature nematic phase was observed in the compound MBBA synthesized by Hans Kelker, but the substance did not qualify for any technological application due to the nar-

row nematic phase range, which was also strongly affected by impurities. The twisted nematic (TN) field effect in liquid crystals was filed for patent on December, 1970 by Hoffmann-LaRoche in Switzerland, (Swiss patent No. 532 261) with Wolfgang Helfrich and Martin Schadt listed as inventors. The invention was later licensed to the Swiss manufacturer Brown, Boveri & Cie which produced displays for wrist watches during the 70's. At the same time, a similar patent was filed by James Fergason, who was working as associate director at the Liquid Crystal Institute of the Kent State University, together with Alfred Saupe (already famous for the ground breaking work on the nematic-isotropic phase tranisition, the Maier-Saupe Theory). In 1971, the company of Fergason ILIXCO produced the first liquid crystal display (LCD) based on the TN effect, which soon superseded the poor-quality DSM types due to their lower operating voltages and lower power consumption. The success of this technology was also possible thanks to the synthesis of stable cyanobiphenyl compounds by George W. Gray in 1973, which exhibited room-temperature nematic phase in a large temperature window. These materials were not only extremely stable, but they also possessed a large positive dielectric anisotropy and strong birefringence thus making them almost ideal for the twisted nematic cell. In the following years, such technology became widespread, mostly in portable devices with small screens such as watches and calculators. In 1981, Epson manufactured the Epson HX-20, the first laptop computer featuring a LCD, while the earliest LCD television, the Casio TV-10, was introduced in 1983. Since then, more and more applications of this particular phase of the matter are discovered, ranging from optics to organic electronic to biosensors.

1.2 General properties of liquid crystals

Liquid crystals are a peculiar state of matter possessing properties of both isotropic liquids and crystals. In isotropic liquids, a partial correlation in positions and orientations is found only at short distances, usually within the first or the second coordination shell. Instead, molecules in a LC phase

are aligned with each other, even at large intermolecular distances. From a macroscopic point of view, LCs behave similarly to isotropic fluids, but molecules can be easily oriented either by applying weak magnetic or electric fields or, if the LCs is placed in a cell of few μm^2 size, by surface treatment of the cell walls, thus showing the typical anisotropy of crystals. Nonetheless, LC molecules mantain rotational and translational freedom and all those properties which are typical of liquids, e.g. they adapt to the shape of their container. Also, LCs possess a viscosity comparable to isotropic fluids, although anisotropic, and can form a free surface characterized by a considerable surface tension.

Liquid crystals can be divided in two main categories: lyotropics and thermotropics. In the former, the type of phase they assume depends on their concentration in a solvent, while the latter undergo phase transitions as the temperature is changed. Among the many LC phases (nematic, smectic, columnar, discotic etc.), we will mainly focus on the nematic and smectic ones, since they will be subject of study in the following chapters.

Nematic phase

Among all the thermotropic phases, the nematic one is probably the most common and important for technological applications (e.g. LCDs). The origin of its name comes from the Greek word $\nu\eta\mu\alpha$ (nema), which means "thread". This term is often used to describe the thread-like topological defects that can be recognized when observing a nematic phase through a polarized light microscope, as shown in Figure 1.1. Threads are analogous to dislocations in solids and are usually referred to as 'disclinations'.

The most peculiar characteristic of this phase is the presence of long-range orientational order, i.e. molecules tend to align their long molecular axis along a preferred direction called director. In absence of external orienting factors, such as an electric field or boundaries, the orientation of the director varies continuously throughout the sample. This is due to the thermal energy which causes fluctuations in the orientation of the molecules as they diffuse through the sample. These director fluctuations in turn modulate the

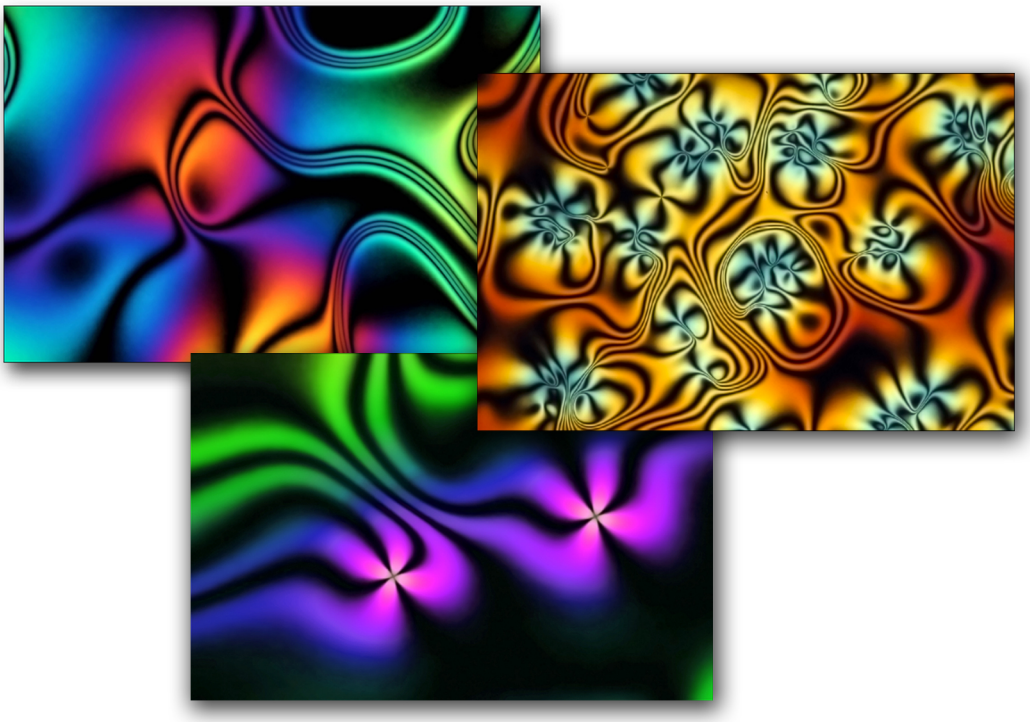

Figure 1.1: Typical schlieren textures of nematic liquid crystals observed through a polarized light microscope.

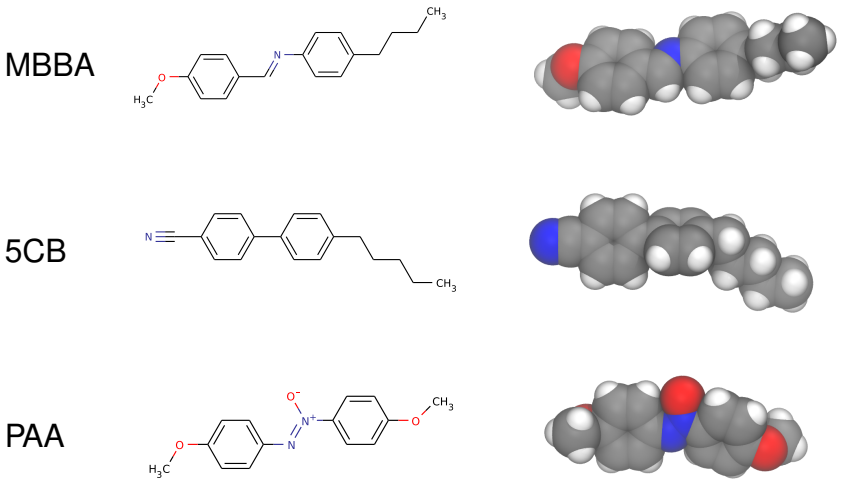

Figure 1.2: Typical liquid crystal compounds: N-(4-Methoxybenzylidene)-4-butylaniline (MBBA), 4-Cyano-4'-pentylbiphenyl (5CB), para-Azoxyanisole (PAA)

refractive index of nematics on a microscopic scale and lead to a strong light scattering, from which their turbid appearance originates. In nematic fluids there is no long-range order in the positions of the center of mass, but a certain amount of short-range organization can be found as in ordinary isotropic liquids. Nematic phases commonly show anisotropy in their physical properties, even though on average such properties usually resemble those of other organic fluids. In Table 1.2 a few common examples of molecules possessing a liquid crystalline phase are reported.

Smectic phase

Smectic phases have further degrees of order compared to the nematic one and are usually found at lower temperatures. The term smectic comes from the greek word $\sigma\mu\eta\gamma\mu\alpha$ (smegma) which means soap, due to the preponderance of soap-like compounds that featured this peculiar phase at the time of their discovery. Smectics have stratified, lamellar structures, with a well defined interlayer spacing. Molecules exhibit some correlations in their positions in addition to the orientational ordering. Given the weakness of

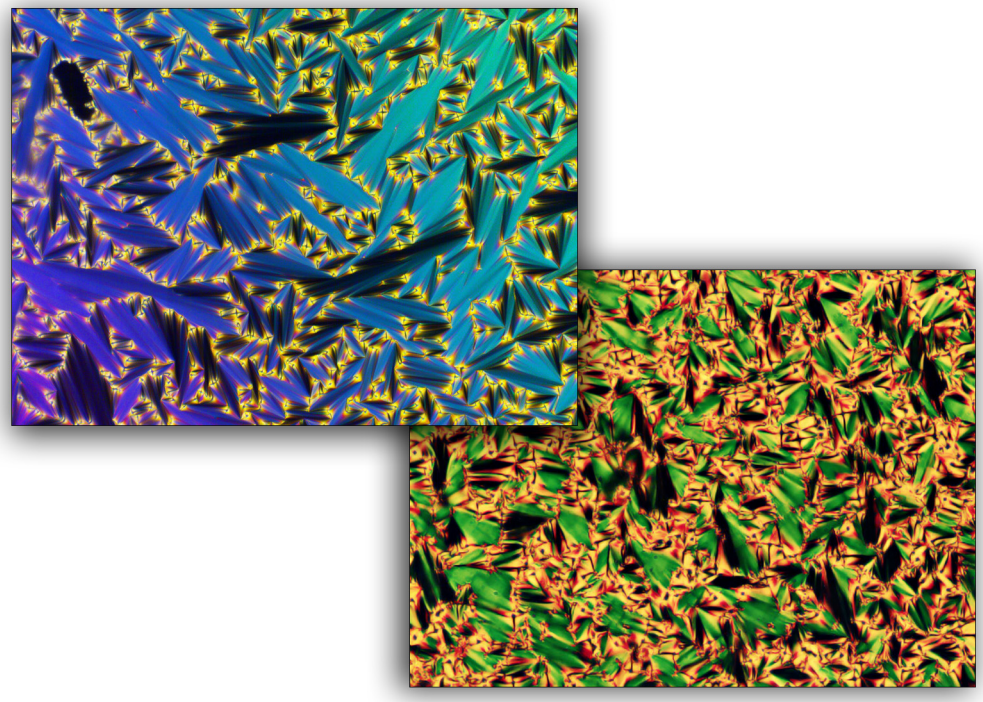

Figure 1.3: Typical focal-conic textures of smectic liquid crystals observed through a polarized light microscope.

the interlayer attractions, layers are able to slide over one another relatively easily, giving rise to a highly viscous fluid system. The smectic phase can be divided in several subgroups, each defined by the extent of the in-plane positional ordering of the molecules and by the orientational order given by the tilt of the long molecular axis with respect to the layer planes.

The simplest structure belonging to this category is the smectic A. In this phase, molecules are arranged in diffuse layers each composed by molecules with their long axis on average perpendicular to the layer planes. Within each layer the molecular center of mass are ordered randomly in a liquid-like fashion and they have considerable translational and rotational freedom around their long-axes. Given the flexibility of layers, distortions are often present in smectic A phases, giving rise to optical patterns known as focal-conic textures, shown in Figure 1.3.

The long molecular axis can be tilted up to 15° from the layer normal, mak-

ing the layer spacing slightly shorter than the molecular length. However, since the tilting occurs randomly across the bulk phase, the direction of the molecules is on average perpendicular to the layer planes thus making the phase uniaxial.

Another common lamellar system is the smectic C one. In this phase, molecules are still arranged in layers, but the orientation of the molecular long axis is tilted at a temperature-depentent angle with respect to the layer planes. Many other types of smectic phases exist (S_B, S_I, S_F, S_L, S_J, S_G, S_E and so on), each featuring either a peculiar molecular orientation or molecular packing. Later in Chapter 4 we will throughly discuss the nature of the smectic A_d phase, which is very similar in nature to the smectic A but is characterized by the presence of bilayers.

Chapter 2

Molecular dynamics simulations

2.1 Introduction

Molecular dynamics (MD) is a computer simulation technique where the time evolution of a set of interacting particles (generally atoms or molecules) is followed step by step by integrating their equations of motion. MD is therefore a deterministic technique if we use a reversible dynamic algorithm: given an initial set of positions and velocities, the subsequent time evolution is completely determined and in principle reversible.
The forces are usually obtained as the gradient of a potential energy function, depending on the positions and possibly on the orientations of the particles. The realism of the simulation therefore depends on the ability of the potential chosen to reproduce the one experienced by the real system under the conditions at which the simulation is run, on the numerical accuracy of the integration of the equations of motions and on the time length explored, which should be chosen in function of the time scale of the studied phenomena.
In a classical MD simulations, forces are derived from classical potentials, i.e. an interaction potential that is a function of the positions of the atoms (molecules), and does not take in account the electrons positions. A quantum MD simulation is one in which the forces can be calculated from both a classical potential and the electronic Schrödinger equation.
While evolving in space through time, the system explores a region of "phase space", the collection of all the configurations or states a system could as-

sume if there were no constraints on it. However, in reality we only consider systems under some forms of constraints, in which case only a region of phase space, called *ensemble*, is accessible. Thermodynamic properties can be obtained by taking their average value throughout the ensemble: this technique is analogous to obtaining ensemble averages based on probability distribution functions and can be rationalized with the help of statistical mechanics theory.

The simulations usually need extensive computer power, and even with the most powerful computers available today it is not possible to calculate the evolution of more than perhaps 10^6 atoms at a time. This is very little, considering that a sample employed to measure experimentally a macroscopic property has a dimension of 10^{20} atoms. Also, depending on system size, it is not possible to simulate processes that last more than one microsecond. In spite of these limitations, molecular dynamics simulations can be used to examine and describe numerous problems in physics and chemistry.

2.2 Historical background

The molecular dynamics method was first introduced by Alder and Wainwright in the late 1950's[1,2]: the purpose of the paper was to investigate the phase diagram of a hard sphere system, and in particular the solid and liquid regions. Many important insights concerning the behaviour of simple liquids emerged from their studies.

In 1960 we find the article "Dynamics of radiation damage" by J. B. Gibson et al.[3] from Brookhaven National Laboratory, that is probably the first example of a molecular dynamics calculation with a continuous potential based on a finite difference time integration method. The calculation for a 500-atoms system was performed on an IBM 704, and took about a minute per time step.

The next major advance was in 1964, when Aneesur Rahman, in his famous paper "Correlations in the motion of atoms in liquid argon"[4], studied a number of properties of liquid Ar, using the Lennard-Jones potential on a sys-

tem containing 864 atoms and a CDC 3600 computer. Rahman's computer codes are still currently employed in many molecular dynamics programs.

In 1967, Loup Verlet calculated the phase diagram of argon using the Lennard-Jones potential, and computed correlation functions to test theories of the liquid state[5,6]. The Verlet time integration algorithm and the trick of keeping a list of the neighbouring particles within the cutoff sphere to speed up the calculation, the so-called Verlet neighbour list, were both introduced in these papers. Phase transitions in the same system were investigated by Hansen and Verlet two years later[7].

The first molecular dynamics simulation of a realistic system was performed by Rahman and Stillinger in their simulation of liquid water in 1974[8], while the first protein simulations appeared in 1977 with the simulation of the bovine pancreatic trypsin inhibitor (BPTI) by McCammon et al.[9].

Nowadays, the number of simulation techniques has greatly expanded and evolved in many specialized techniques for particular problems, including mixed quantum mechanical - classical simulations[10]. Molecular dynamics simulations are being widely used to study the physics and the chemistry of materials (liquids, liquid crystals, crystals, proteins, membranes, surfaces, clusters, defects, friction, fracture), and are proving day by day to be a useful, everyday all-purpose tool also for the experimental researcher.

2.3 Hamiltonian dynamics

The trajectory of a system can be followed with the help of Hamiltonian dynamics. Hamiltonian dynamics was introduced in 1834 as a generalization of Newton's equations for a point particle in a force field; virtually all of the fundamental models in physics are described by such dynamics.

Because of Hamilton's equations being of first-order, and due to the symmetry between momenta and positions, the Hamiltonian formulation is easier to simulate numerically than other formulation such as the Euler-Lagrange.

The Lagrangian of a system is defined as

$$L = T - V \tag{2.1}$$

where T is the total kinetic energy and V is the total potential energy. Given a Lagrangian L, we can define the Hamiltonian of a system as

$$H(\mathbf{q}, \dot{\mathbf{q}}, t) = \sum_{i=1}^{n} (\dot{q}_i p_i) - L(\mathbf{q}, \dot{\mathbf{q}}, t) \tag{2.2}$$

where q_i is a generalized coordinate, $\mathbf{p}_i$ is a generalized momentum, that for most of the studied systems correspond to position r_i and momentum $\mathbf{p}_i = m_i \mathbf{v}_i$, with m_i being the mass of the i-th particle moving at the velocity $\mathbf{v}_i$. If L is a sum of functions homogeneous (i.e., no products of different degrees) in generalized velocities of degrees 0, 1, and 2 and the equations defining the generalized coordinates are not functions of time, then the Hamiltonian can be expressed as follows:

$$H = T + V = E \tag{2.3}$$

where T is the kinetic energy, V is the potential energy, and E is the total energy of the system.

As p_i and q_i are conjugate variables, an Hamiltonian system has always and even number of dimensions $2N$, therefore N integrals are necessary to specify a trajectory, following Hamilton's equations:

$$\dot{q}_i = \frac{\partial H}{\partial p_i} \tag{2.4}$$

$$\dot{p}_i = -\frac{\partial H}{\partial q_i} \tag{2.5}$$

$$\dot{H} = -\frac{\partial L}{\partial t} \tag{2.6}$$

These equations have fixed points when

$$\dot{q}_i = \frac{\partial H}{\partial p_i} = 0 \tag{2.7}$$

$$\dot{p}_i = -\frac{\partial H}{\partial q_i} = 0 \tag{2.8}$$

In other words an equilibrium point is found when $\nabla H = 0$, i.e. when the system reaches a critical point of the total energy function H.

A Hamiltonian system is *conservative*, as the energy is invariant along the trajectories:

$$\begin{aligned} \frac{dH}{dt} &= \sum_{i=1}^{n} \left(\frac{\partial H}{\partial q_i} \frac{\partial q_i}{\partial t} + \frac{\partial H}{\partial p_i} \frac{\partial p_i}{\partial t} \right) \\ &= \sum_{i=1}^{n} \left(\frac{\partial H}{\partial q_i} \frac{\partial H}{\partial p_i} - \frac{\partial H}{\partial p_i} \frac{\partial H}{\partial q_i} \right) \\ &= 0 \end{aligned} \tag{2.9}$$

It can also be proved that Hamiltonian flows are volume preserving. From these properties of the Hamiltonian systems it follows that the trajectories obtained belongs to the microcanonical (NVE, with constant number of molecules, volume and energy) ensemble.

2.4 Integration of the equations of motion

Solving the equations of motion requires a numerical integration of the differential equations. The integration is typically done by discretizing the variable t in small timesteps dt using finite difference methods. These are explicit methods, based on a Taylor expansion of the positions and momenta at a time $t + dt$ (Equation 2.10), that use the state of the system at a time t to predict the state at a time $t + dt$:

$$\begin{aligned} \mathbf{r}(t+dt) &= \mathbf{r}(t) + \dot{\mathbf{r}}(t)dt \; + \; \frac{\ddot{\mathbf{r}}(t)}{2}dt^2 \; + \; ... \\ &= \mathbf{r}(t) + \mathbf{v}(t)dt \; + \; \frac{\mathbf{f}(t)}{2m}dt^2 \; + \; ... \end{aligned} \tag{2.10}$$

2.4.1 Verlet integrator

The most common integration algorithm in Molecular dynamics is the Verlet integrator[5], which is based on the addition of two Taylor expansions in time, one forward and one backward:

$$\mathbf{r}(t+dt) = \mathbf{r}(t) + \mathbf{v}(t)dt \; + \; \frac{\mathbf{f}(t)}{2m}dt^2 \; + \; ... \tag{2.11}$$

$$\mathbf{r}(t-dt) = \mathbf{r}(t) - \mathbf{v}(t)dt \; + \; \frac{\mathbf{f}(t)}{2m}dt^2 \; + \; ... \tag{2.12}$$

$$\mathbf{r}(t+dt) = 2\mathbf{r}(t) + \mathbf{r}(t-dt) \; + \; \frac{\mathbf{f}(t)}{2m}dt^2 \; + \; O(dt^4) \tag{2.13}$$

Advantages and drawbacks of Verlet's algorithm are the following:

- Integration does not require the velocities, which are nevertheless required for the calculation of the energy. These can be extimated with the formula obtained subtracting the expansion above:

$$\mathbf{v}(t) \; = \; [\mathbf{r}(t+dt) + \mathbf{r}(t-dt)]/(2dt) \tag{2.14}$$

- Only a single evaluation of forces is required at each time step.

- The formulation is time reversible.

- Rather large numerical errors, due to the addition of an $O(dt^0)$ term $[2\mathbf{r}(t) + \mathbf{r}(t-dt)]$ to an $O(dt^2)$ term $[\frac{\mathbf{f}(t)}{m}dt^2]$.

2.5 Constant temperature molecular dynamics

As we have seen before, Hamilton equations lead to a trajectory in the microcanonical (NVE) ensemble. To run simulations in other ensembles, some tricks of the trade, or some modification of the Lagrangian are needed. Simulating a system at constant temperature, thus in a canonical (NVT) ensemble, has the thermodynamical meaning of bringing the system into thermal contact with a large heat bath. In any case the simulation temperature can be calculated from the average kinetic energy of the system $\langle K \rangle = {}^1\!/_2\, mv^2$:

$$\frac{3}{2}NkT = \langle K \rangle \tag{2.15}$$

$$T = \frac{2}{3k}\langle K \rangle = \frac{1}{3kN}\langle \sum m_i v_i^2 \rangle \tag{2.16}$$

2.5.1 Constant kinetic energy methods

The simplest way to perform simulations at constant temperature is to rescale all the velocities in order to keep kinetic energy constant. It is a very crude approach that consists in a periodic scaling of all the particle velocities of a factor $(\frac{T_{ext}}{T})^{\frac{1}{2}}$, where T is the instantaneous system temperature, calculated from equation 2.16, and T_{ext} is the temperature of the thermal bath. This technique is also often used to equilibrate systems during the the first few hundred MD steps before the production run starts and data are collected.
A more gentle way, known as Berendsen or weak-coupling thermostat[11], is to use a factor that depends on the deviation of the instantaneous kinetic energy K from the average value K_0, corresponding to desired temperature T_0. At each time step velocities are scaled by the factor λ:

$$\lambda^2 = 1 + \frac{dt}{\tau_T}(\frac{K}{K_0} - 1) \tag{2.17}$$

where dt is the MD time step, and τ_T is a parameter that defines the strength of the coupling with the thermostat and has the dimension of a time.

Both methods do not reproduce canonical ensemble, as the condition of constant average kinetic energy does not correspond to the condition of constant temperature, i.e. the fluctuations of the temperature and kinetic energy follow different laws. Nevertheless, these methods lead to trajectories whose average values correspond to the ones of the canonical enseble, even if their fluctuations do not[12,13].

2.6 Constant pressure molecular dynamics

It is also possible to run simulations in NPT and NPH ensembles, corresponding to isobaric and isoenthalpic conditions respectively.
The system pressure tensor $\mathbf{\Pi}$ is measured as sum of the kinetic energy contribution (ideal gas contribution, always positive) plus the interparticle energy contribution (the so called virial tensor,$\mathbf{W}$). The pressure P is then calculated from the trace of the pressure tensor:

$$P = \frac{1}{3}Tr(\mathbf{\Pi}) \tag{2.18}$$

$$\mathbf{\Pi} = \frac{1}{V}\left[\sum_{i}^{N} m_i(v_i \otimes v_i) + \mathbf{W}\right] \tag{2.19}$$

$$\mathbf{W} = \sum_{i=1}^{N} \mathbf{r}_i \otimes \mathbf{f}_i \tag{2.20}$$

If a cutoff scheme is used, the virial must be calculated from the pairwise forces instead of being calculated from the total force acting on each particle (see reference[14]):

$$\mathbf{W} = \sum_{i=1}^{N} \sum_{j>i} \mathbf{r}_{ij} \otimes \mathbf{f}_{ij} \tag{2.21}$$

The barostat formulations generally mimic the ones derived for thermostats: in particular, the most used barostats are again the weak-coupling barostat and the more elegant Parrinello–Rahman[15].

2.6.1 Weak coupling barostat

The weak coupling scheme can be also applied to couple the system to a "pressure bath"[11]. Once fixed the desired external pressure P_{ext}, the task can be accomplished by periodically rescaling all center of mass coordinates and box size, either isotropically or anisotropically, following a first order relaxation law:

$$\frac{dP}{dt} = \frac{P_{ext} - P}{\tau_P} \tag{2.22}$$

$$P(t + \Delta t) = P(t) + (P_{ext} - P(t))\frac{\Delta t}{\tau_P} \tag{2.23}$$

In the first case, the coordinate scaling factor μ is given by:

$$\mu = \left[1 + \frac{\Delta t}{\tau_P}\beta(P - P_{ext})\right]^{\frac{1}{3}} \tag{2.24}$$

where τ_P is the pressure coupling time constant (usually $\approx$ 1ps) and β is the experimental isothermal compressibility of the system. When the latter is not known, it is common pratice to use water compressibility ($\beta_{H_2O} = 4.5^{-10}\ Pa^{-1}$), as β influences only the pressure fluctuations frequency and not the pressure itself, and as many liquids have similar values.

To obtain an anisotropic coupling and eventually run a simulation with non-orthogonal box, one must deal with the 3×3 matrix $\mathbf{h}$, whose lines are the vectors defining the simulation cell and whose determinant is the cell volume.

The variation matrix $\mathbf{M}$ is then obtained from the the pressure tensor:

$$\mathbf{M} = \left[\frac{\beta}{\tau_P}(\mathbf{\Pi} - P_{ext}\mathbf{I})\right] \tag{2.25}$$

The new (scaled) $\mathbf{h}$ matrix is given by:

$$\mathbf{h}(t + \Delta t) \;=\; \mathbf{h}(t) + \mathbf{M}\,\mathbf{h}(t) \tag{2.26}$$

The coordinates scaling is then accomplished as follows:

$$\mathbf{r}_{scaled} \;=\; \mathbf{h}(t + \Delta t)\,\mathbf{h}^{-1}(t)\,\mathbf{r} \tag{2.27}$$

2.7 Finite size effects and boundary conditions

The finite–size of the simulated sample introduces systematic deviations from bulk (infinite) behaviour. In order to reduce their influence on simulations, we employ the common artifact of periodic boundary conditions (PBC). This way, the simulation box is replicated in all directions to form an infinite lattice (see Figure 2.1); in this way, the volume of interaction around each particle has the same geometry as the sample cell.

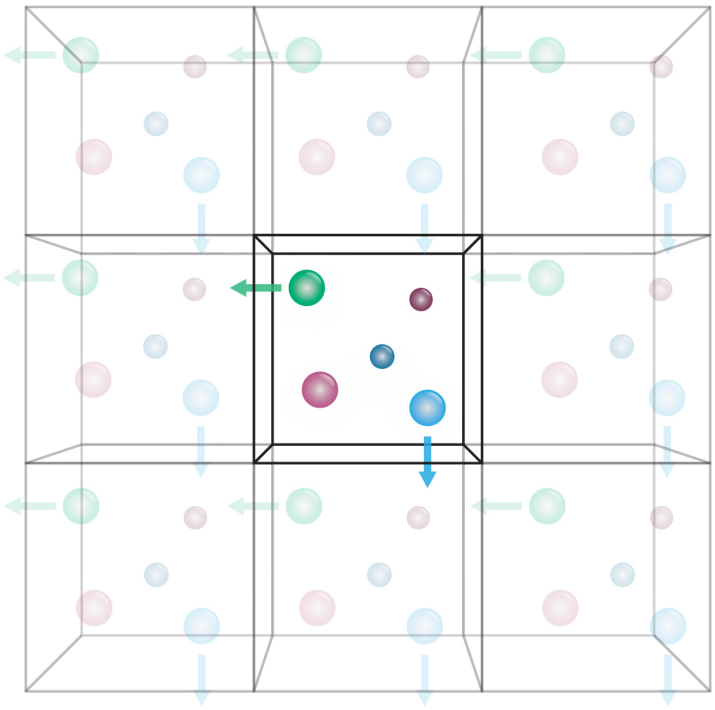

Figure 2.1: Graphical representation of periodic boundary conditions

In the course of the simulation, as a molecule moves in the original box, its periodic images in each of the neighbouring boxes move in the same way. Thus, if a molecule leaves the central box, one of its images will enter through the opposite face. In this way, the system does not present free surfaces, even if we have introduced an additional spurious periodic correlation between the particles. In the case of a short range intermolecular potential this does not constitute a problem; indeed if the range of the molecular interaction is less than half side length, the central box comprises all interactions and we use the *minimum image convenction*, that is, the distance between two different particles i and j is taken as the distance between i and the nearest image of j[16]. Thus every particle i interacts only with the nearest image of another molecule j. In practice, most simulations evaluate potentials using some cutoff scheme for computational efficiency: each particle does not interact with all the nearest images of the other $N-1$ particles, but only with those minimum images contained in a sphere of cut-off radius R_c centered at the particle. It is therefore assumed that the interactions are negligible outside the sphere volume.

Chapter 3

Force fields for molecular simulations

3.1 Molecular mechanics

Theoretical studies of molecules allow to analyze the relationships between structure, function and dynamics at the atomic level. Since the majority of the problems that one would like to address in complex chemical systems involve many atoms, it is not yet feasible to treat these systems using quantum mechanic (QM) methods.

The answer to the need of high detail at low computational cost is Molecular Mechanics (MM), a technique which uses classical mechanics to analyze the structure and dynamics of molecular systems.

Within this approximation, the molecule is treated at the atomic level, i.e. the electrons are not treated explicitly. The energy and the forces are calculated through a given potential energy function, or *force field* (FF), which is translationally and rotationally invariant and depends on the relative positions of the atoms and on a small number of parameters that have been determined either experimentally or via quantum mechanical calculations. In this way, given a particular conformation or configuration, the energy of the system can be calculated straighforwardly.

The interatomic interactions are typically described by simple two-, three-,

and four-body potential energy functions. This classical force field-based approach is a great simplification over quantum chemistry, which describes systems in terms of nuclei, electrons, and wavefunctions. This simplicity allows molecular mechanics to be applied to much larger systems than those that can be studied by QM methods.

Current generation force fields provide a reasonably good compromise between accuracy and computational efficiency. They are often calibrated to experimental results and quantum mechanical calculations of small model compounds. The development of parameter sets is a very laborious task, requiring extensive optimization. This is an area of continuing research and many groups have been working over the past two decades to derive functional forms and parameters for potential energy functions of general applicability to biological molecules.

During the past ten years, several force fields have been developed for protein simulations, such as CHARMM[17], GROMOS[18] and OPLS/AMBER[19,20] force fields, while the UFF[21] and MM3[22] force fields are more likely used to study small, isolated molecules. Most recent force fields that have obtained some success are the NERD[23] united atom FF for hydrocarbons and the very complex, yet effective, COMPASS force field[24].

The most important limitation of traditonal force fields is that no drastic changes in electronic structure are allowed, i.e., no events like bond making or breaking can be modeled. If one is interested in treating chemical reactions, a quantum mechanical treatment or an alternative, new formulation of force fields is necessary, like the REAXFF one[25].

Recent developments regarding force fields are currently focused on the explicit inclusion of the electronic polarization for the treatment of nonbonded interactions, leading to the so called polarizable or non additive force fields. This in principle will allow to simultaneously treat molecules in environments with significantly different polar character with high accuracy[26].

3.2 The potential

The typical potential energy function is a sum of diverse bonded and non–bonded contributions, each of them containing a sum over the atoms or groups of atoms.

$$U_{\text{total}} = U_{\text{bonds}} + U_{\text{angle}} + U_{\text{dihed}} + U_{\text{LJ}} + U_{\text{charge}} \tag{3.1}$$

$$U_{\text{bonds}} = \sum_{\text{bonds}} K_r^{t_i t_j} (r_{ij} - r_{eq}^{t_i t_j})^2 \tag{3.2}$$

$$U_{\text{angles}} = \sum_{\text{angle}} K_\theta^{t_i t_j t_k} (\theta_{ijk} - \theta_{eq}^{t_i t_j t_k})^2 \tag{3.3}$$

$$U_{\text{dihed}} = \sum_{\text{dihed}} V_\phi^{t_i t_j t_k t_l} [1 + \cos(n^{t_i t_j t_k t_l} \phi_{ijkl} - \gamma^{t_i t_j t_k t_l})] \tag{3.4}$$

$$U_{\text{LJ}} = 4 \sum_{i<j} f_{LJ}^{1,4} \, \epsilon_{t_i t_j} \left[\left(\frac{\sigma_{t_i t_j}}{r_{ij}} \right)^{12} - \left(\frac{\sigma_{t_i t_j}}{r_{ij}} \right)^{6} \right] \tag{3.5}$$

$$\text{where} \qquad \epsilon_{t_i t_j} = (\epsilon_{t_i} \epsilon_{t_j})^{\frac{1}{2}} \, , \; \sigma^{t_i t_j} = \frac{\sigma_{t_i} + \sigma_{t_j}}{2}$$

$$U_{\text{charge}} = \sum_{i<j} f_q^{1,4} \, \frac{q_i q_j}{r_{ij}} \tag{3.6}$$

The terms contributing to the energy reported above are common to the majority of the currently used force fields, including CHARMM, AMBER, GROMOS, OPLS among others. The variables contained in Equations 3.2–3.6 are distances r_{ij}, angles θ_{ijk} and dihedral angles ϕ_{ijkl}; all the other terms are force field parameters.

The first ‘bonded’ sum is over bonds between atom pairs; the second sum is over bond angles defined by three atoms; the third sums is over atom foursomes. In the ‘nonbonded’ interactions (Lennard Jones and electrostatics), the summation is over atom couples i and j, where $i < j$ simply ensures that each interaction is counted only once. Generally, atoms separated by one or two bonds are excluded from the nonbonded sum, and those separated by three bonds, the so called ‘1-4 interactions’, may have nonbonded interactions reduced by a multiplicative scale factor ($f_{LJ}^{1,4}$,$f_q^{1,4}$). For bookkeeping purposes, each atom is assigned a number, but it is unlikely to have specific

parameters for each atom; instead the force fields are based on the concept of atom types (t_i,t_j), i.e. a set of parameters defined for a chemical type of atom that can possibly used in the MM description of a class of molecules, rather than for a single molecular specie (e.g. methylene carbon or aromatic carbon are typical atom types).

3.3 Bonded interactions

This type of interactions has the main purpose of correctly describing the equilibrium geometry of the molecule, but to a certain extent also to reproduce its conformational space. The description of bonded interactions is based on the molecular topology, i.e. on a fixed connection matrix, making this approach clearly not feasible to describe chemical reactions. As a convention, the bonded energy minimum is set as zero, so the bonded energy is always positive. Bonded interactions are represented schematically in Figure 3.1.

3.3.1 Bonds and angles

The standard way to approximate the potential energy for a bond in molecular mechanics is to use a Hooke's law term:

$$U_{\text{bond,Hooke}} = K(r_{ij} - r_{eq})^2 \tag{3.7}$$

where r_{ij} is the distance between the two bonded atoms i, j, r_{eq} is the equilibrium bond length and K is a force constant.
The shape of the potential energy well will be parabolic (see Figure 3.2) and the motion will therefore tend to be harmonic. This kind of approach does not attempt to reflect the energy of formation of the bond - it only seeks to reflect the energy difference on a small motion about the equilibrium value. A much more accurate representation of the bond stretching is based on the application of the Morse potential, which has an anharmonic potential

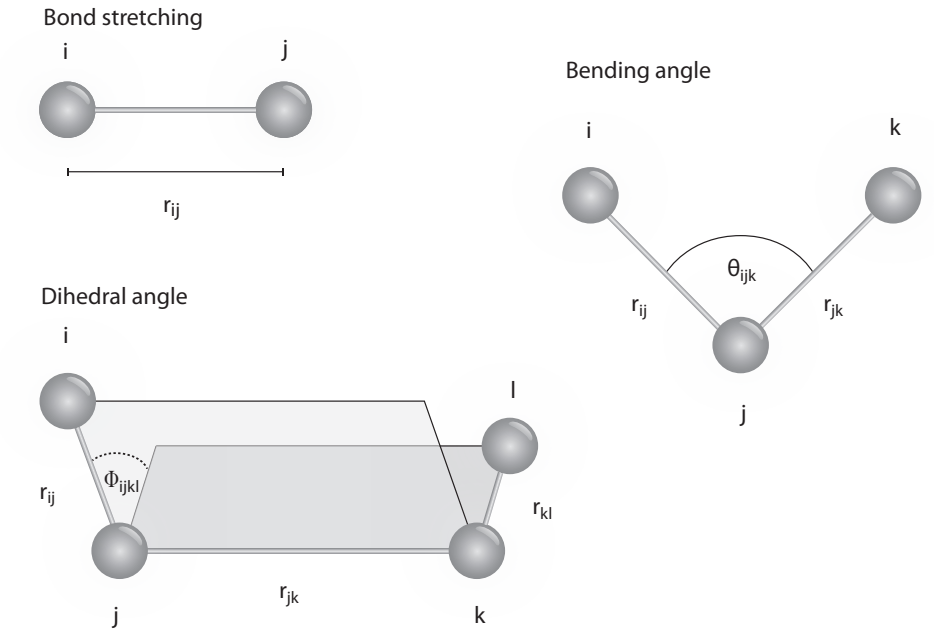

Figure 3.1: Graphical representation of bonded interactions.

energy well as shown in Figure 3.2.

$$U_{\text{bond,Morse}} \;=\; D_e[1 - e^{-(r_{ij} - r_{eq})}]^2 \tag{3.8}$$

where D_e is the "equilibrium" dissociation energy of the molecule (measured from the potential minimum). This formulation is not commonly used for applications in which the main focus is on the study of structural details, but is necessary if one is interested in spectroscopic applications.

A bond angle between atoms i-j-k is defined as the angle between the bonds i-j and j-k. As bond angles, in a similar manner to bond lenghts, are found, experimentally and theoretically, to vary around a single value, it is sufficient in most applications to use an harmonic representation in order to provide an accurate description:

$$U_{\text{angle}} \;=\; K_\theta^{t_i t_j t_k}(\theta_{ijk} - \theta_{eq}^{t_i t_j t_k})^2 \tag{3.9}$$

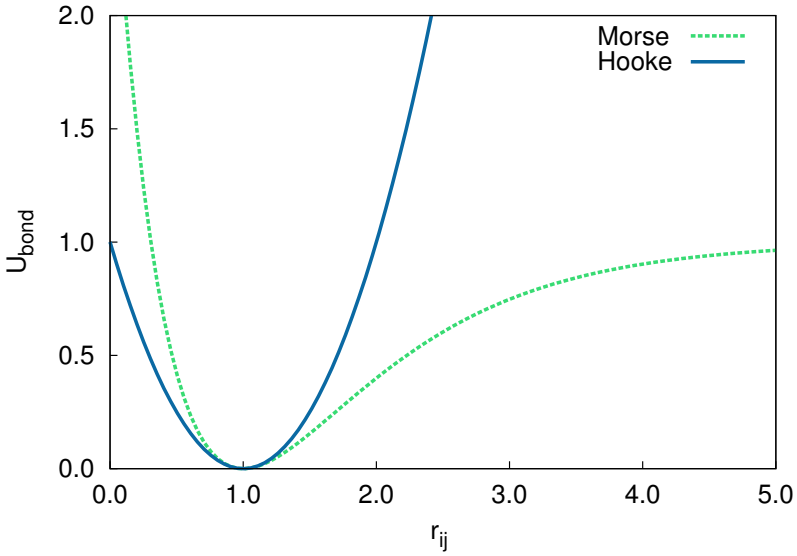

Figure 3.2: Morse potential with $D_e = 1$, $r_e q = 1$ and best fitting Hooke potential in the interval $r_{ij} \in [0.6, 1.4]$ ($K = 1.0003$)

3.3.2 Torsion angles

Torsion angles are distinguished in two brands: dihedral or proper torsion angles and improper torsion angles.

Formally, the dihedral angle (also known as a torsion angle) between four atoms i-j-k-l is defined as the angle between the planes ijk and jkl (see Figure 3.1). The angle can vary from -180 to 180, and its sign is taken as the one of the scalar product $(\mathbf{n}_{ijk} \times \mathbf{n}_{jkl}) \cdot \mathbf{r}_{jk}$, where the $\mathbf{n}$ are the normal to the planes.

The standard functional form for representing the potential energy for a torsional rotation was introduced by Pitzer[27]:

$$U_{\text{dihed}} = V_\phi[1 + \cos(n\ \phi_{ijkl} - \gamma)] \tag{3.10}$$

where V_ϕ is the half energy barrier to rotation, n is the number of maxima (or minima) in one full rotation and γ determines the angular phase. Barriers for dihedral angle rotation can be attributed to the exchange interaction of electrons in adjacent bonds and to steric effects.

The Pitzer potential is insufficient to give a full represention of the energy barriers of a dihedral angle change. Modern potential energy functions normally model the dependence of the energy on dihedral angle change by a combination of truncated Fourier series and non-bonded effects.

Improper torsions are named so because the atoms involved are not serially bonded but rather branched, and the form of the potential used is the same employed for bond angles (Equation 3.10).

The convention is that the central atom is listed in the third position of the dihedral, and the order of the other three is determined alphabetically by atom type - and when types are the same, by atom number (order in the molecule).

Improper dihedral potentials are sometimes necessary to reproduce out-of-plane bending frequencies, i.e. to keep four atoms properly trigonal planar for a two-fold torsional potential. They are additionally used in the united-atom force field model when a carbon with an implicit hydrogen is a chiral center, thus preventing an unphysical inversion of chirality.

3.4 Nonbonded interactions

The number of valence interactions that must be calculated for a molecule is usually proportional to the number of atoms N_A. The number of nonbonded terms, however is roughly proportional to N_A^2, since they involve almost all possible pairs of atoms, except the ones bonded, directly or in α, one to each other.

Despite the systematic use of cutoffs, for large systems the bulk of computational time is spent calculating the nonbonded interactions, thus great efforts have been made to optimize these calculations for vector and parallel processors.

3.4.1 Charges

Electrostatic forces are of paramount importance in determining intermolecular interactions. The most common approach to include their contribution in a simulation is to place a charge at each atomic center (nucleus). The charge can take a fraction of an electron and can be positive or negative. Charges on adjacent atoms (joined by one or two covalent bonds) are normally made invisible to one another, since the interactions between these atoms are taken into account by the bonded interaction term.
The electrostatic attraction or repulsion between two charges is described by Coulomb's law:

$$U_{\text{charge}} = \frac{1}{4\pi\epsilon_0\epsilon_r}\frac{q_i q_j}{r_{ij}} \tag{3.11}$$

where q_i and q_j are the atoms partial charges, r_{ij} is the distance separating the atom centers, ϵ_0 is the permittivity of free space, and ϵ_r is the relative dielectric coefficient of the medium between the charges (often taken as one).
Using partial charges at nuclear centres is the crudest effective abstraction. To obtain a more accurate representation, two approaches are commonly used: the first is to add dipole, quadrupole and higher moments to the nuclear centres; the second is to introduce further non-nuclear centres. This is commonly done to represent the anisotropy in a potential caused by lone pairs on oxygen atoms[28].
In many respects, electrostatic interactions represent the biggest problem to computational studies of soft matter, as, by their nature, they are long range and dependent on the properties of the surrounding medium.

3.4.2 Lennard–Jones

The equilibrium distance between two proximal atomic centers is determined by a trade off between an attractive dispersion force and a core-repulsion force that reflects electrostatic repulsion.
The Lennard-Jones potential represents a successful effort in reproducing

this balance with a simple expression:

$$U_{\mathrm{LJ}} \;=\; 4\epsilon\left[\left(\frac{\sigma}{r_{ij}}\right)^{12} - \left(\frac{\sigma}{r_{ij}}\right)^{6}\right] \;=\; \frac{A}{r_{ij}^{12}} - \frac{B}{r_{ij}^{6}} \tag{3.12}$$

where σ is the contact distance (where $U_{\mathrm{LJ}}(\sigma) = 0$) and ϵ is the well depth (where $\partial U_{\mathrm{LJ}}/\partial r_{ij} = 0$).

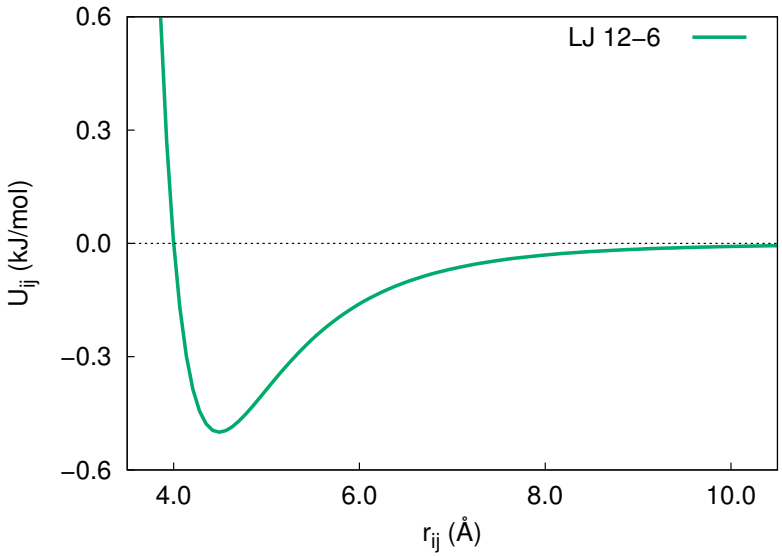

Figure 3.3: Typical LJ potential used in atomistic simulation: the impossibility of taking a cutoff lower than 9 is apparent.

The term r_{ij}^{-12} dominating at short distance, models the repulsion between atoms when they are brought very close to each other. Its physical origin is related to the Pauli principle: when the electronic clouds surrounding the atoms starts to overlap, the energy of the system increases abruptly. The exponent 12 was chosen exclusively on a practical basis, as it is particularly easy to compute, knowing the attractive term. In fact, on physical grounds an exponential behavior would be more appropriate, as represented in the Buckingham potential, used in simulations of solids:

$$U_{\mathrm{Buckingham}} \;=\; A\exp(-Br_{ij}) - \frac{C}{r_{ij}^{6}} \tag{3.13}$$

The term r_{ij}^{-6}, dominating at large distance, constitutes the attractive part.

This is the term which gives cohesion to the system and originates from van der Waals dispersion forces rising from dipole-dipole interactions which are due to fluctuating dipoles. These are rather weak interactions, which however dominate the bonding character of closed-shell systems, that is, rare gases such as Ar or Kr, and also apolar solvents.
For simplicity, Lennard-Jones forces are typically modeled as effectively pair-wise additive, and the rules to calculate the mixing parameters for couples of different atom types, are simple as well. Nonetheless, one of the major issue that limits the possibility to mix LJ parameters from different force fields originates from the different combining rules employed to compute such interactions. These rules are used to take LJ parameters σ_i and r_i for an individual atom i and combine them with the ones of an atom j in order to yield the LJ$_{ij}$ interaction for a specific atom pair. Unfortunately, each force field employs a different way to combine parameters. For example, CHARMM and AMBER obtain the combined σ_{ij} value via geometric mean and the r_{ij} value via arithmetic mean, while OPLS combines both parameters through geometric mean. In cases where the combining rules for two force fields are different, it is typically not recommended to transfer parameters between the two force field, since this could lead to unexpected, non-realistic results.
For its simplicity and effectiveness, LJ is the standard potential used for all the investigations where the focus is on fundamental issues, rather than studying the properties of a specific material.

Chapter 4

Atomistic simulations of bulk 8CB

4.1 Introduction

Nowadays, atomistic simulations of condensed matter, and of LCs in particular, offer a view with an unprecedent level of detail on the molecular organization and dynamics, allowing to inspect for the first time the role of specific molecular features like internal flexibility and dipoles on the phase behaviour[29–34].

Compared with generic models, like the Gay-Berne one[35,36], where the mesogen molecule is replaced by a single rigid object, the atomistic level of description grants us the access to those chemical details needed to predict or at least interpret the results of x-ray diffraction, nuclear magnetic resonance (NMR) and other real experiments. For instance, several works published in the last few years have proved that "in silico" nematics like cynnamates[29] and cyanobiphenyls[29,37] can reproduce a large number of experimental results like transition temperatures, density, order parameters, NMR dipolar couplings and can help to interpret the origin of phenomena like the odd-even effect, i.e. the alternation in nematic-isotropic transition temperatures determined by the variation of the number of aliphatic carbon atoms in homologue series of these LC compounds.

It is also worth pointing out that atomistic simulations have a significant predictive value: for example, values of the fourth rank orientational order pa-

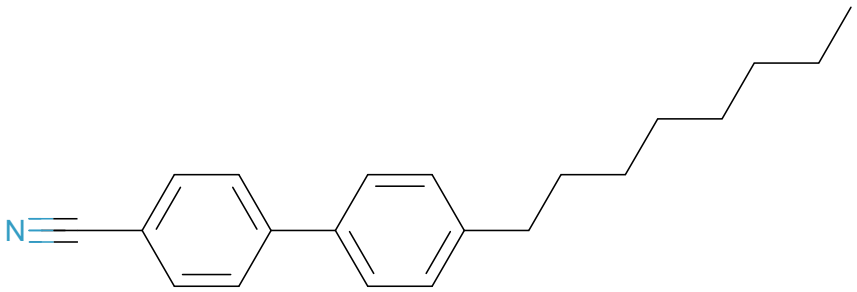

Figure 4.1: Structural formula of 8CB (4 n octyl - 4′cyanobiphenyl)

rameter $\langle P_4 \rangle$ obtained for 4 n pentyl - 4′ cyanobiphenyl (5CB) were at variance with those available at the time of publication[38], but have proved in good agreement with those recently obtained using an improved version of the same depolarized Raman scattering technique[39]. The comparison with experimental evidences is not always straightforward, given the large scattering found among measurements published by different groups, even when the same analytical technique was used.

While the quality of observable results obtained from MD is approaching that of real experiments for nematics, much less is known on the possibility of reproducing smectic molecular organizations and properties.

From this point of view, 4 n octyl - 4′cyanobiphenyl (8CB, whose structural formula is shown in Figure 4.1) is an ideal test bench since it has been the subject of numerous experimental investigations and of some of the first atomistic simulations a few years ago[40], even though these simulations were started assuming molecular positions already placed in layers and the trajectories were followed for a time lower than the expected rotational relaxation time for a molecule of that size.

More recently, several groups have reported their results regarding simulations of the 8CB bulk phase. McDonald and Hanna[41], employing a united atom (UA) level of modeling, succesfully obtained a smectic phase but did not reproduce the dimerization of 8CB molecules and the transition temperatures. Prampolini[42] and coworkers, employing a mixed UA – all atoms model, found the spontanous onset of a partial bilayer smectic phase in a temperature range compatible with the experimental evidence, but the layer spacing was still slightly far from the one obtained by X-ray measurements

and the limited number of simulations did not allow to precisely assess the transition temperatures.
It remains to be verified whether a smectic organization similar to the real one (in terms of layer spacing, transition temperatures etc.) can be obtained by simply cooling an isotropic liquid.
Here, we take advantage of a recently developed force field for cyanobiphenyls[29]. One of the significant issues we plan to investigate is the type and extent of antiparallel arrangement for these molecules with a strong terminal dipole[43].

4.2 Methods and computational details

Each simulated sample was composed of 750 molecules of 8CB, corresponding to 16500 interaction centers, and was modelled at united atoms (UA) level of detail using a AMBER-OPLS force field[44,45], which was previously tuned to reproduce the experimental nematic-isotropic transition of n-alkyl cyano biphenyls with 5 to 8 carbon atoms in the linear alkyl chain[46] but was that not optimized for the smectic phase.
We decided to perform our simulations according to a previously established procedure[34,46,47]: we started from a temperature at which the sample is isotropic and then progressively cooled it at lower temperatures, allowing to observe, if present, its spontaneous organization. To study the 8CB liquid crystalline phases, we ran a series of MD–NPT simulations using NAMD[48] with multiple step integration: bonded, van der Waals and electrostatic interactions were calculated every 2, 4 and 8 fs respectively. The sample was kept at the constant pressure of 1 atm using a Berendsen barostat[49], while the temperature, which ranged from 300 to 320 K, was kept constant through velocity rescaling. Three dimensional periodic boundary conditions were used and long range electrostatic interactions were computed through the Particle Mesh Ewald method[50] with the grid spacing set to 1.2 Å.
The average simulation runtime for each sample was about 150 ns long, a time much larger than the expected rotational and translational decay time. It

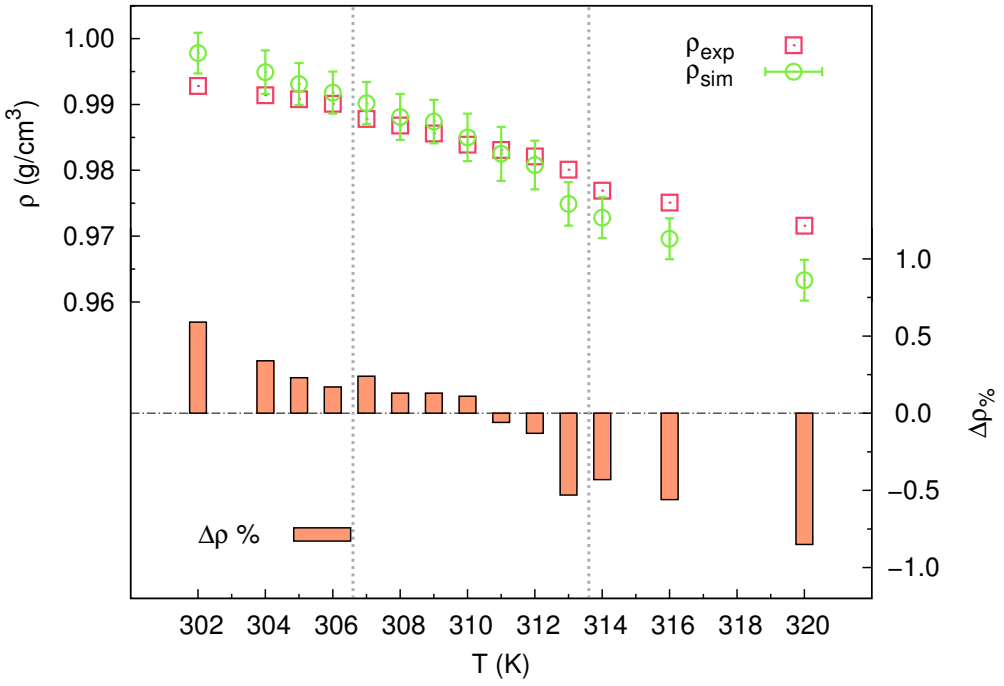

Figure 4.2: Comparison between experimental and simulated density as a function of temperature. $\Delta\rho_{\%}$ is the percent deviation of the simulated density from the experimental value. Vertical dashed lines represent the experimental transition temperatures T_{SmN} and T_{NI}.

is worth noting that for samples at temperatures close to a phase transition, we prolonged the production time up to 400 ns.

4.3 Results and discussion

4.3.1 Density

A preliminary validation of our results can be found comparing density values obtained by our simulations with the experimental ones available in literature[51] (Figure 4.2).

The simulated density decreases while the sample is heated, reproducing precisely the experimental trend, like already shown in reference[46] for smaller samples composed of 250 molecules. Still in Figure 4.2, it can be

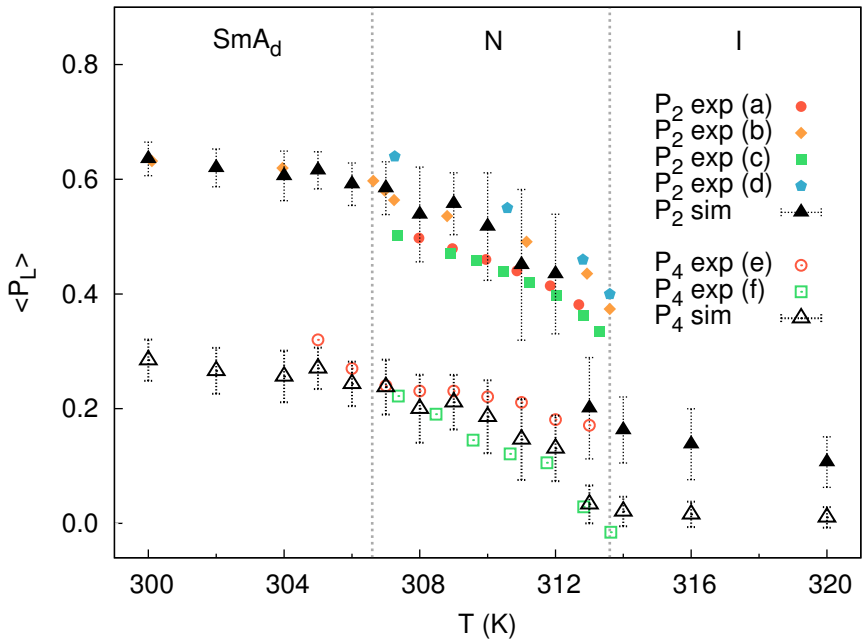

Figure 4.3: Nematic order parameters $\langle P_2 \rangle$ and $\langle P_4 \rangle$ of the simulated samples compared with different sets of experimental data as a function of temperature.
(a-c) data from refractive index measurements in references[52–54] and (d -f) from polarised Raman spectroscopy measurements in references[38,55]

noticed how the most accurate results are obtained in proximity of the experimental nematic-isotropic transition temperature T_{NI}, with a deviation from experiment not greater than 0.1%. Moving away from the transition region, this discrepancy increases to 1%, though these results still qualify as accurate.

4.3.2 Orientational order

The liquid crystalline phase of 8CB presents two different mesophases in a very narrow temperature range. In particular, the smectic-nematic and nematic-isotropic transition temperatures (T_{SmN} and T_{NI}), which will be represented as vertical dashed lines in the following figures, are located at 306.6 and 313.6 K respectively. The presence of an order-disorder thermotropic phase transition can be easily identified observing the variation

with temperature of a suitably defined orientational order parameter, such as $\langle P_2 \rangle$ for nematic-isotropic transitions. This is calculated through a standard procedure for liquid crystal studies, which requires to build and diagonalize an order matrix $\mathbf{Q}$, summing over all N molecules of the sample:

$$\mathbf{Q}(t) = \frac{1}{2N} \sum_{I=1}^{N} \left[3\mathbf{u}_I(t) \otimes \mathbf{u}_I(t) - \mathbf{I} \right], \tag{4.1}$$

where $\mathbf{u}_I(t)$ is the chosen reference molecular axis and $\mathbf{I}$ is the identity matrix. The instantaneous order parameter $P_2(t)$, which corresponds to the value of P_2 for each configuration, can be obtained from the eigenvalues $\lambda_-(t) < \lambda_0(t) < \lambda_+(t)$ of the $\mathbf{Q}$ matrix. According to the most common convention, $P_2(t)$ corresponds to the largest eigenvalue, which is to say $P_2(t) = \lambda_+$, and once a sufficiently long trajectory is available, the time average $\langle P_2 \rangle$ is calculated.

As can be seen in Figure 4.3, at high temperatures the samples possess a very low value of $\langle P_2 \rangle$, ranging from 0.1 to 0.2. Between 313 and 312 K we observe a steep rise of the order parameter, suggesting a spontaneous onset of a nematic phase. In fact, after the isotropic-nematic transition, $\langle P_2 \rangle$ increases from 0.4 to slightly less than 0.6 as we move toward the nematic-smectic transition.

Still in Figure 4.3, the results obtained by our simulations can be compared with different sets of experimental data, in particular with birifringence and Raman depolarization spectroscopy measurements[38,52–54]. We notice that data obtained from our simulations are in good agreement with the average of the various, rather scattered experimental data sets.

The nematic-isotropic transition is characterized by considerable oscillations of $\langle P_2 \rangle$, with a standard deviation comparable to the value of the order parameter itself (cf the error bars in Figure 4.3). This is due to the presence of oder-disorder fluctuations during the time evolution of the sample, each denoted by either high or low P_2 values. That explains the high uncertainity on P_2 values calculated at 311-313 K and is consistent with the first order nature of the NI transition.

We arbitrarily choose to consider a phase as “nematic” when it shows a

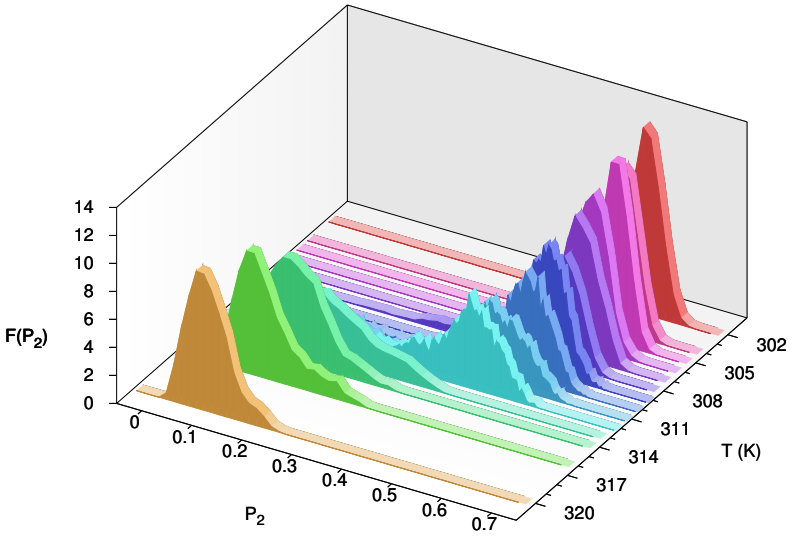

Figure 4.4: Distribution histograms of the istantaneous values of P_2 at different temperatures.

$\langle P_2 \rangle$ greater than 0.3, hence locating T_{NI} between 312 and 313 K. This assumption can be confirmed by observing the distributions of $\langle P_2 \rangle$ at each temperature (Figure 4.4), which allow to easily spot the temperature at which the nematic transition takes place. For temperatures above 313 K, it can be noticed how every sample possesses a broad distribution of $\langle P_2 \rangle$, with a peak close to 0, highlighting how most of the molecules in those samples possess isotropic $\langle P_2 \rangle$ values.

On the other hand, below 312 K peaks look sharper and are shifted toward high values of the order parameter, as a consequence of the onset of highly ordered liquid crystalline phases such as the nematic and smectic ones. The sudden inversion of the population of molecules possessing high or low $\langle P_2 \rangle$ values happening between 313 and 312 K confirms once again our estimate of the transition temperature, which is closer to the experimental value[56] of 313.6 K with respect to previous simulations performed on samples of 250 molecules (317 K). This also shows the importance of the sample size, which must be sufficiently large in order to accurately locate phase transitions. Below 308 K, the order parameter is almost constant with

the temperature and its fluctuations become much smaller thus leading to sharper distributions.

The orientational order of the simulated samples was further investigated by studying the fourth rank order parameter $\langle P_4 \rangle$, which contains information of the fourth moment of the orientational distribution and that can be calculated as follows:

$$\langle P_4 \rangle = \frac{1}{8N} \sum_{i=1}^{N} \langle 35 \cos^4 \beta - 30 \cos^2 \beta + 3 \rangle, \tag{4.2}$$

where β is the angle between the reference axis of the i molecule and the istantaneous phase director, computed as the eigenvector of $\mathbf{Q}(t)$ with the largest eigenvalue. The value of $\langle P_4 \rangle$ at each temperature is compared in Figure 4.3 with experimental data from Raman depolarization measurements[55]: it can be seen that the experimental trend is again well reproduced by simulations. Moreover, the profile of the fourth rank order parameter follows closely the one observed for $\langle P_2 \rangle$, dropping to zero above 312 K and thus confirming our previous estimate of the transition temperature.

4.3.3 Radial distributions

In order to characterize 8CB mesophases, it is convenient to evaluate also the positional order of the sample. In particular, we considered the radial distribution function:

$$g_0(r) \quad = \quad \frac{1}{4\pi r^2 \rho_N} \langle \delta(r - r_{IJ}) \rangle_{IJ}, \tag{4.3}$$

where $\mathbf{r}_{IJ}$ is the vector corresponding to the distance lying between the reference centers of the I and J molecules and $\rho_N = N/V$ is the number density of the sample. $g_0(r)$ is calculated considering the charge centre of molecules as the reference centre. Figure 4.6 shows the radial distributions of the smectic, nematic and isotropic phases. It can be seen that each phase has a liquid-like distribution, characterized by the absence of peaks in the

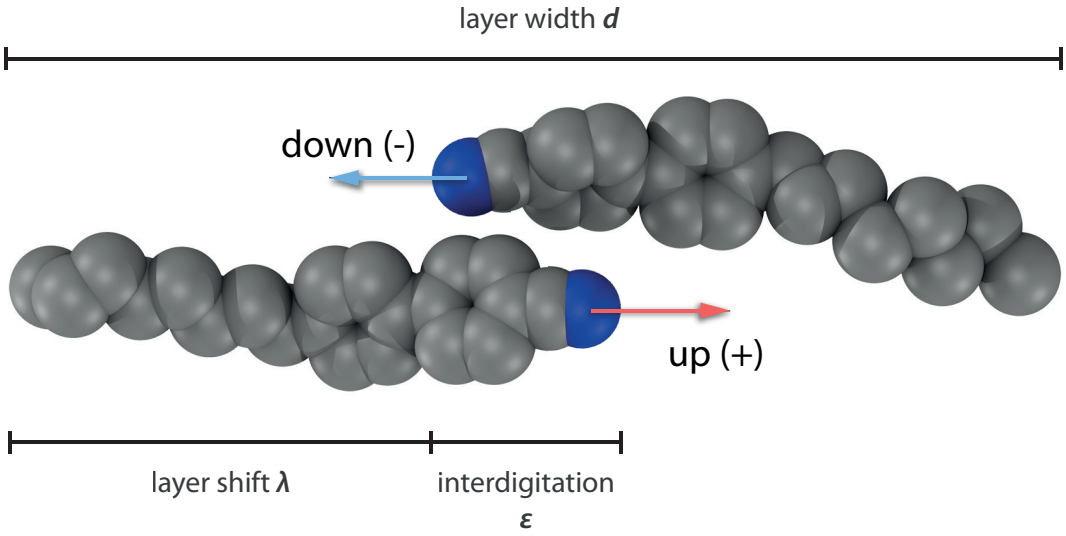

Figure 4.5: Orientational and positional arrangement of two molecules isolated from the smectic sample at 304 K. $\mathbf{d}$ is the layer spacing and $\varepsilon = d - 2\lambda$ is the layer interdigitation.

long range region and tending asymptotically to 1 for r greater than 30 Å. In the short range region though, each system shows three distinct peaks, indicating the presence of local coordination shells. In particular, the first peak located at 3.8 Å suggests the presence of quasi dimeric associations (as shown in Figure 4.5) in both the isotropic and anisotropic phases, a common feature for systems made of molecules bearing a strongly polar group such as the cyano group. When the temperature is raised, the short range structure becomes less definite as shown by the radial density distribution of the isotropic sample.

The following step in the evaluation of the positional-orientational order was to combine the knowledge of both the radial distribution and the molecular orientations in order to obtain radial orientational correlation functions:

$$g_1(r) = \langle \delta(r - r_{IJ})(\hat{\mu}_I \cdot \hat{\mu}_J) \rangle_{IJ}, \tag{4.4}$$

$$g_2(r) = \langle \delta(r - r_{IJ}) \left[\frac{3}{2}(\hat{\mu}_I \cdot \hat{\mu}_J)^2 - \frac{1}{2} \right] \rangle_{IJ}, \tag{4.5}$$

where $\hat{\mu}_I, \hat{\mu}_J$ are the electric dipole unit vectors and r_{IJ} is the distance be-

tween the charge centres of I and J molecules.

In particular, the $g_1(r)$ function shown in Figure 4.6 allows to clarify the local polar order generated by dipole alignment. In the short range region, a negative value for $g_1(r)$ is expected, since the first neighbouring molecules are paired in an antiparallel fashion, thus yielding a negative average of $\hat{\mu}_I \cdot \hat{\mu}_J$. At a somewhat greater distance, a change of sign of $g_1(r)$ is observed, since those molecules belonging to the next coordination shell are parallel to the ones in the first shell (but antiparallel to the reference molecule). Between 8 and 14 Å, we observe the same trend described for the first and second neighbours, but less pronounced since the influence of the reference molecule gets weaker as the distance increases. At long range, the value of $g_1(r)$ tends asymptotically to 0 as the interaction with the reference molecular dipole becomes negligible, therefore leading to a statistical orientation of the most distant molecules.
The $g_2(r)$ function allows to evaluate the relative order parameter P_2 of a molecule with respect to the orientation of the reference molecule as a function of the intermolecular distance. Figure 4.6 clearly shows the presence of a peak in the short range region, corresponding to the orientational order raising from the short range interactions, in analogy with the behaviour of isotropic fluids[37,43,57]. At greater distances, in our case for r > 30 Å, $g_2(r)$ decreases and tends asymptotically to the $\langle P_2 \rangle^2$ of the phase.

4.3.4 Positional order and density profiles

The analysis of the molecular mass center distribution is also useful to verify the formation of a smectic phase, that experimentally occurs below 306.6 K[56] for 8CB. For this purpose, we plot in Figure 4.7 the linear density distribution normalized to the average density of the sample $g(z) = \rho(z)/\rho_0$, where z is the layer normal, which in this case corresponds also to phase director. It is evident that at low temperatures the density profile has an ondulatory trend, due to the presence of smectic layers. This behaviour progressively vanishes for samples at temperatures above 307 K, even though

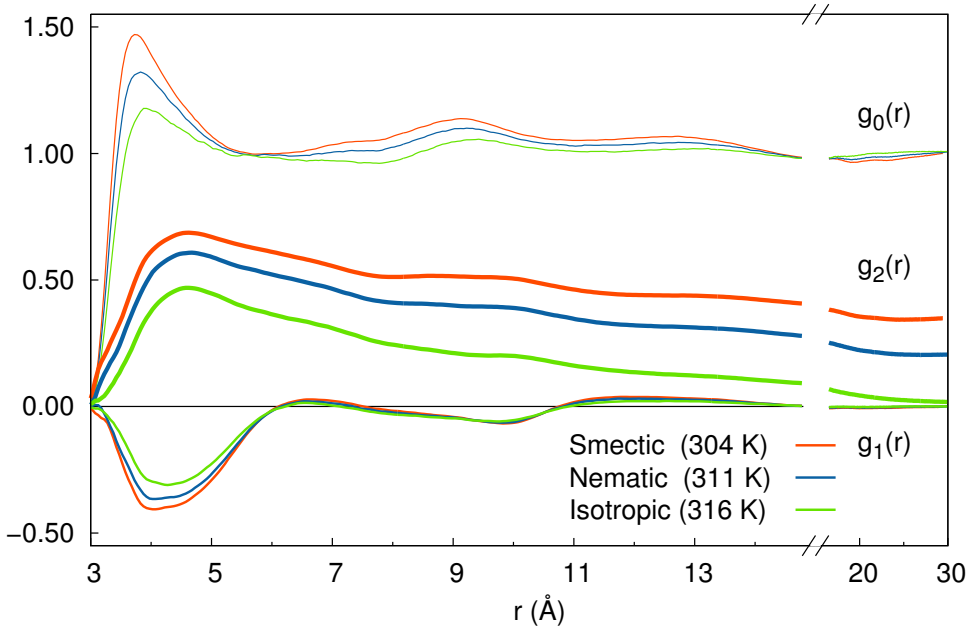

Figure 4.6: Dipole-dipole orientational correlation functions $g_1(r)$, $g_2(r)$ and of the radial density distribution of centers of charge $g_0(r)$ for samples at 304, 311 and 316 K (representing the smectic, nematic and isotropic phases respectively).

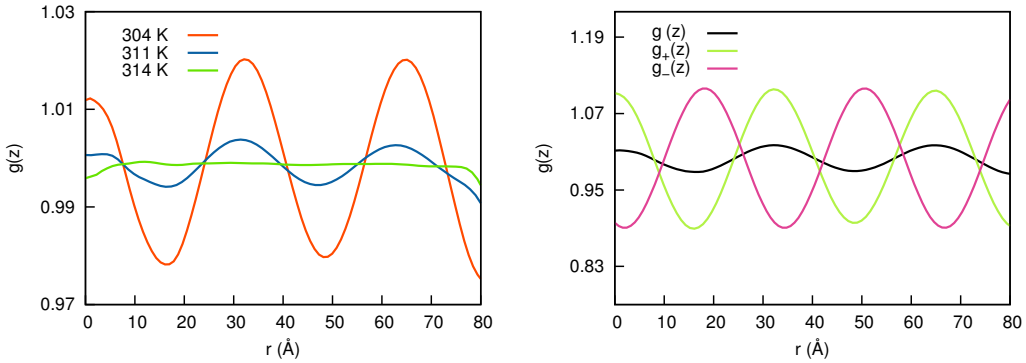

Figure 4.7: On the left, trend of the normalized density distribution along the z axis for samples at 304, 311 and 316 K (representing the smectic, nematic and isotropic phases respectively). On the right, comparison of up and down molecules density profiles $g_{\pm}(z)$ with the one of the whole sample $g(z)$ at the temperature of 304 K.

an evident discontinuity is not present, suggesting a second order nature for the transition between the nematic and the smectic phase.

The smectic phase of 8CB, which belongs to the SmA_d[58] category, is characterized by the presence of bilayers formed by two interdigitated sublayers of molecules oriented in opposite directions in order to optimize the interaction between the polar groups. In particular, 8CB bilayers are commonly described as *partial*, since the distance d between bilayers is lower than twice the molecular length l, differently from smectics composed by single layers, where d is about as large as l[58]. In particular, the distance measured experimentally between 8CB layers is 31.4 Å[59], that is approximately 1.5 times the length of onw molecule.

For a matter of convenience, in the following paragraphs we referer to molecules forming the sublayers either as *up(+)* or *down(-)* molecules, depending on whether their dipolar vector is parallel or antiparallel to the arbitrarily chosen layer normal direction.

The snapshot in Figure 4.8 shows the evident interdigitation between up and down (red and blue) molecules forming the bilayer of the simulated sample, which faithfully reproduces the disposition of molecules in a real sample.

In the simplest case[60,61], the normalized density profile along the layer normal director z of a non tilted smectic sample (Figure 4.7) can be approxi-

mated with the following sinusoidal function:

$$g(z) = \frac{\rho(z)}{\rho_0} \approx 1 + A\cos qz, \tag{4.6}$$

where $q = 2\pi/d$, with d being the interlayer distance, and where A represents the amplitude of oscillations - here being either the smectic order parameter $\langle\tau\rangle = \langle\cos qz\rangle$, if we are referring to the whole sample, or $\langle\tau_\pm\rangle$ if we consider up/down molecules only. Values of $\langle\tau\rangle$ and $\langle\tau_\pm\rangle$ calculated by fitting the density distribution profiles with Equation 4.6 are reported in Table 4.1. As shown in Figure 4.7, both + and - profiles have exactly the same trend, but they are shifted by a certain phase $q\lambda$. Once λ and d values are known, we will be able to determine the bilayer interdigitation ε (Figure 4.5). The normalized total density profile is given by the superposition of the up and down density waves, provided they are suitably shifted:

$$\begin{aligned} g(z) &= \frac{1}{2}[g_+(z) + g_-(z+\lambda)] \\ &= 1 + \frac{1}{2}\langle\tau_\pm\rangle[\cos q(z - \frac{\lambda}{2}) + \cos q(z + \frac{\lambda}{2})], \end{aligned} \tag{4.7}$$

Equation 4.7 reproduces the density profile of the whole sample (Figure 4.7) and features a maximum located at $z = 0$, thus we used it to fit the density profiles of the samples, determining the values of d, λ and hence the interdigitation ε, reported in Table 4.1.
Once derived the value of d and λ, it is possible to obtain an estimate of $\langle\tau\rangle$ directly from $\langle\tau_\pm\rangle$ by combining Equations 4.6 and 4.7:

$$\langle\tau\rangle = \langle\tau_\pm\rangle \cos\pi\frac{\lambda}{d}, \tag{4.8}$$

The presence of the smectic-nematic transition is denoted by a sudden fall of the smectic order parameter $\langle\tau\rangle$ and a slight inflection of the interlayer distance d above 307 K, in very good agreement with the experimental smectic-

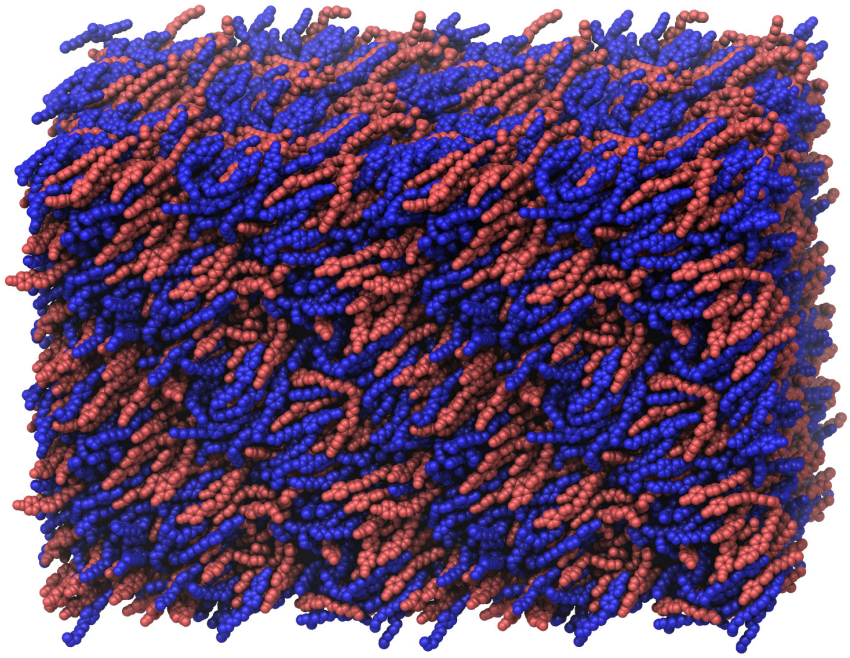

Figure 4.8: Layer interdigitation in a smectic sample at 304 K (replicated twice along x, y and z axes). Red and blue colors represent parallel and antiparallel molecules.

nematic transition temperature of 306.6 K. It is worth noting that smectic fluctuations are present also in the whole nematic phase, in agreement with experimental x-ray measurements[62,63].

Below 307 K, the samples we simulated feature an average interlayer distance d of about 32.4 Å (see Table 4.1), which is much closer to the experimental value[62] of 31.7 Å with respect to previous simulation studies[41,42,64]. Besides, the interlayer distance obtained from simulations remains constant in the temperature range of the smectic phase, in agreement with the trend found experimentally through X-ray measurements by Urban and coworkers[65].

4.3.5 Diffusion in the smectic phase

Since we are dealing with a fluid of anisotropic nature, it is of interest to evaluate the behaviour of translational diffusion tensor components D_{ii} in function of the temperature, hence in each different phase (in particular in

Table 4.1: Simulated values with respect to the temperature of: density ρ - nematic order parameter $\langle P_2 \rangle$ - from density distribution fits with Equation 4.6 and 4.7: smectic order parameters τ and $\tau_{\pm}$, interlayer distance d, shift between up and down sublayers λ, sublayer interdigitation ε - average value of the length to breadth molecular aspect ratio l/w, calculated from the dimensions of the minimal rectangular box containing the molecule rotated in its inertial frame[29] - diffusion coefficients from simulations in $10^{-10} m^2/s$: isotropic, parallel and perpendicular coefficients D_{iso}, $D_{\parallel}$ and $D_{\perp}$.

T (K)	ρ (g/cm^3)	$\langle P_2 \rangle$	$\tau \times 10^2$	$\tau_{\pm} \times 10^2$	d (Å)	λ (Å)	ε (Å)	l/w	D_{iso}	$D_{\parallel}$	$D_{\perp}$
300	1.000	0.64	2.7	16	32.3	14.4	3.5	3.35	2.6	3.8	1.9
302	0.998	0.62	2.2	12	31.8	14.0	3.8	3.37	2.6	3.9	2.0
304	0.995	0.61	2.1	11	32.4	14.2	4.0	3.36	2.8	4.1	2.1
305	0.993	0.62	3.3	17	32.5	14.3	3.9	3.36	2.8	3.9	2.2
306	0.992	0.59	2.5	12	32.6	14.3	4.0	3.35	3.0	4.4	2.3
307	0.990	0.58	2.1	12	32.6	14.3	4.0	3.34	3.0	4.3	2.3
308	0.988	0.54	0.9	5	31.9	14.0	3.9	3.33	3.3	4.8	2.6
309	0.987	0.56	1.1	6	31.6	14.0	3.6	3.16	3.4	4.9	2.6
310	0.985	0.52	1.0	5	31.8	14.1	3.6	3.32	3.6	5.2	2.8
311	0.982	0.45	0.4	2	31.3	14.0	3.3	3.28	3.8	5.4	3.1
312	0.981	0.43	0.2	1	31.2	14.8	1.6	3.28	4.0	5.5	3.2
313	0.975	0.20	-	-	-	-	-	-	4.4	-	-
314	0.973	0.16	-	-	-	-	-	-	4.5	-	-
316	0.970	0.14	-	-	-	-	-	-	4.8	-	-
320	0.963	0.11	-	-	-	-	-	-	5.4	-	-

the SmA_d one), in order to further validate the simulation results through the comparison with dynamics experimental data[66]. D_{ii} can be calculated from the mean square positional fluctuations using the classic Einstein formula:

$$D_{ii} = \lim_{t\to\infty} \frac{\langle (r_i(0) - r_i(t))^2 \rangle}{2t}, \tag{4.9}$$

where r_i is the component along the axis $i = x, y, z$ of the director frame of the molecular position vector for each molecule, and with the limit for $t \to \infty$ approximated to the value of $t = 10$ ns. The parallel and perpendicular diffusion coefficients $D_{\parallel}$ and $D_{\perp}$ correspond to D_{zz} and $(D_{xx} + D_{yy})/2$ respectively, while the isotropic diffusion coefficient D_{iso} was calculated as $(D_{xx} + D_{yy} + D_{zz})/3$. It is known that for molecules modeled at UA level of detail, the calculated diffusion coefficients are usually higher than experimental values[46,64] as a result of the smoother molecular surface, and such case applies to our sample. While this prevents us from performing a direct comparison with experimental results, we can at least confront the trend of our results and the anisotropy of the diffusion tensor.

The simulated and experimental isotropic diffusion coefficients have an Arrhenius temperature dependence:

$$D_{iso} = D_0 e^{-\frac{E_a}{RT}}, \tag{4.10}$$

where D_0 is the diffusion coefficient for $T \to \infty$ and E_a is the activation energy required for molecules to get over the potential barrier encountered while moving across the sample.

We perform a linear interpolation of the diffusion coefficients, obtaining a simulated activation energy $E_{a,sim}$ equal to 34.0 kJ mol^{-1}, very close to the experimental value[66] $E_{a,exp}$ of 34.2 kJ mol^{-1}, and a $D_{0,sim}$ of 1.97$\times 10^6$ m^2/s against the experimental value we extrapolated from the NMR work of A. Maliniak and coworkers[66]($D_{0,exp} \sim$ 1.96$\times 10^5$ m^2/s). As previously noted, the D_0 value obtained from simulations is greater than the one from real samples, in this case being roughly one order of magnitude higher with re-

spect to experimental results.

To increase the predictivity of the force field with regard to the dynamic properties (e.g. viscosity or relaxation times), it can be useful to have a function that, given a simulated diffusion coefficient, returns a rescaled one directly comparable to experimental values. For this purpose, we define two rescaling factors:

$$\alpha = \frac{D_{0,exp}}{D_{0,sim}}, \quad \beta = \frac{E_{a,exp}}{E_{a,sim}}, \tag{4.11}$$

which in our case correspond to $\alpha = 0.1$ and $\beta = 1.01$, that we employed in the following expression:

$$D_{iso,sr} = \alpha e^{(1-\beta)\frac{E_{a,sim}}{RT}} D_{iso,sim}, \tag{4.12}$$

where $D_{iso,sr}$ is the simulation-rescaled isotropic diffusion coefficient. We applied Equation 4.12 not only to rescale the isotropic coefficient, but also to $D_{\parallel}$ and $D_{\perp}$. The rescaled coefficients $D_{iso,sr}$, $D_{\parallel,sr}$ and $D_{\perp,sr}$ can be compared to the experimental data in Figure 4.9.It is important to note that this approach works best at rescaling isotropic diffusion coefficients and it may fail when applied to parallel and perpendicular diffusion coefficients for anisotropic phases. In particular, the Arrhenius equation does not hold at temperatures close to a transition or when a smectic phase is present. Since the nematic temperature range for 8CB is extremely narrow, we cannot safely rely on Equation 4.10 to interpolate $D_{\parallel}$ and $D_{\perp}$ in both nematic and smectic ranges, nor we should use Equation 4.12 to apply a rescaling. To overcome this issue, we employed the Chu and Moroi (CM) model[67], which allows us to compute $D_{\parallel}$ and $D_{\perp}$ for nematic phases as follows:

$$D_{\parallel} = \langle D_{iso} \rangle \left[1 + 2\langle P_2 \rangle \frac{1-\rho}{2\rho+1} \right], \tag{4.13}$$

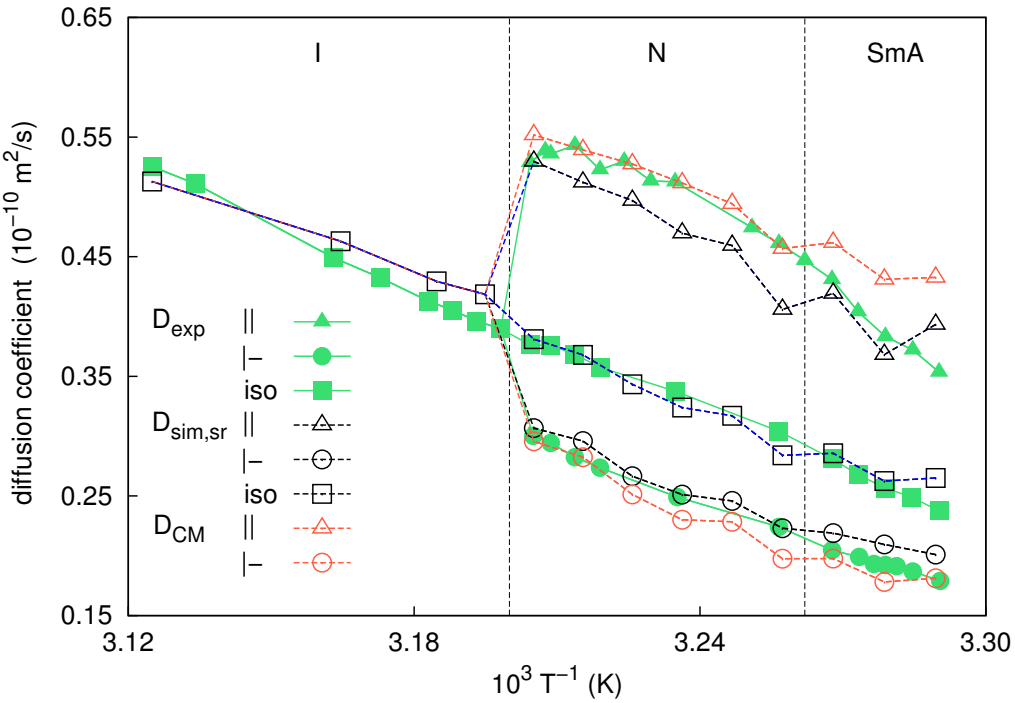

Figure 4.9: Arrhenius plot of simulation-rescaled and experimental diffusion coefficients. Green filled symbols represent experimental values, blue empty symbols represent rescaled values from simulations, orange empty symbols represent values calculated with CM model. Dashed lines correspond to the transition temperatures.

and

$$D_{\perp} = \langle D_{iso} \rangle \left[1 - \langle P_2 \rangle \frac{1-\rho}{2\rho+1} \right], \tag{4.14}$$

where ρ=$\pi d/(4L)$ is a geometrical factor for rod-like molecules of diameter d and lenght l. Thanks to the CM model, once $D_{iso,sim}$, $\langle P_2 \rangle$ and ρ at each temperature are determined from the simulation, we are able to obtain rescaled parallel and perpendicular diffusion coefficients $D_{\parallel,CM}$ and $D_{\perp,CM}$ in the nematic phase using Equations 4.12-4.14. It should be noted that we used the CM model to compute diffusion coefficients even for samples at temperatures below 307 K, though more complex models which take into account the presence of a periodic potential along the director in smectic phases would suit better for the task[68]. This approximation can be made given the low smectic order parameter of 8CB, which should not lead to tangible deviations.

In Figure 4.9 we reported a comparison between the simulation-rescaled and experimental diffusion coefficients. It can be seen that, once adequately rescaled, the diffusion coefficients of simulated samples accurately fit the experimental trend. Moreover, it can be noticed that there is only a slight difference between the values of $D_{\parallel}$ and $D_{\perp}$ calculated from our rescaling and those predicted by the CM model, the latter method being more effective for $D_{\parallel}$.

As common for nematic phases, diffusion along the director is faster compared to the one in the direction perpendicular to the director. This behaviour is inherited by the smectic phase, without showing any sign of discontinuity in correspondence of the smectic-nematic transition. This trend might seem surprising considering the nature of a smectic phase, as one would expect a lower diffusion along the director due to the presence of an interlayer potential. Nevertheless, it has been reported several times in previous experimental[69–71] and computational[32,40] studies that materials with weak smectic-nematic transitions exhibit a smectic phase with a nematic-like diffusional behaviour.

4.4 Conclusions

The liquid crystalline nematic and smectic phases of 4 n octyl - 4′cyanobiphenyl were investigated with atomistic Molecular Dynamics simulations, by performing a progressive cooling of an isotropic sample composed by 750 molecules. Both the isotropic-nematic and nematic-smectic transition temperatures were reproduced in very good agreement with experimental values available in the present literature[56]. We observed the spontaneous onset of a smectic phase, which we thoroughly studied and characterized by determining its density, orientational and positional order and its dynamic properties. In particular, we found the smectic character of 8CB to be weak, with low values of the smectic order parameter. The interlayer distance exhibited by our samples is in very good agreement with the experimental value[62] and we succeded in measuring the sublayer interdigitation. The diffusion coefficients, although being faster of an order of magnitude, can be used to closely reproduce the experimental trend[66] with a method that we introduced employing pre-existing theoretical models.

Chapter 5

Atomistic simulations of 8CB thin films

5.1 About freely suspended smectic thin films

A unique property of smectic liquid crystals is their ability, due to the layered structure, to form stable films that are freely suspended or free-standing over an aperture in a frame. This property has been known since the beginning of the last century. However, it was not until the 1970s that smectic membranes found extensive usage in experimental studies[72–74]. In such films, smectic layers align parallel to the two interfaces with air, which are flat because the surface tension minimizes the surface area of the film. Apart from the edges, such films can be considered as substrate-free. Thus in essence they can be seen as membranes consisting of parallel stacks of smectic layers. Such systems have a high degree of uniformity: the alignment of the smectic layers is almost perfect, allowing the study of single-domain samples of various thicknesses. The surface area can be as large as a thousand mm^2, while the thickness can be easily varied from thousands of layers (tens of μm) down to two layers (about 5 nm). Membranes thicker than several hundred layers can be considered as bulk systems. In addition, in liquid crystals (and thus in smectic membranes) a free surface may stabilize a higher-ordered phase that is only found at lower temperatures or not observed at

all in the bulk. This is in contrast to solids, which exhibit surface-induced disorder that can lead to surface melting[75]. In the case of liquid crystals, surface freezing occurs instead. Outside the field of liquid crystals surface freezing is a rare phenomenon found only in some long-chain alkanes and alcohols[76]. Smectic membranes can be controlled to an extent that is rare for physical systems. In combination with the just mentioned properties, this makes them ideal models for studying low-dimensional fluctuation behavior and phase transitions, which have almost no equivalent in any other type of system and more generally the variation of properties from bulk to film as the number of layers decreases.

5.2 Methods and simulation details

5.2.1 Sample preparation

In order to simulate a sufficient number of layers without excessively reducing the horizontal cell section, we decided to perform the simulations on a larger system compared to the one studied in Chapter 4; thus we duplicated the cell composed of N=750 molecules obtaining a larger sample of N=1500 molecules. In order to simulate an infinite planar film in a vacuum environment, we enlarged the heigth of the cell leaving empty space above and below the film, which is instead periodic in the xy plane. Given the impossibility of using planar periodic boundary condition in combination with the Particle Mesh Ewald (PME) method[48], the height of the cell was adjusted so that no significant interaction was present between replicas on the z axis (Figure 5.1). To test such condition, we run several simulations studying the variation of the potential energy of the system as the z side of the cell was increased. Leaving 600 Å of empty space above and below the film leads to a 0.06% increment of potential energy with respect to only 50 Å, therefore we opted for an average of 300 Å as a good compromise between avoiding spurious interactions between periodic images along the z axis and the increase of computational time, since the cost of PME method scales with the

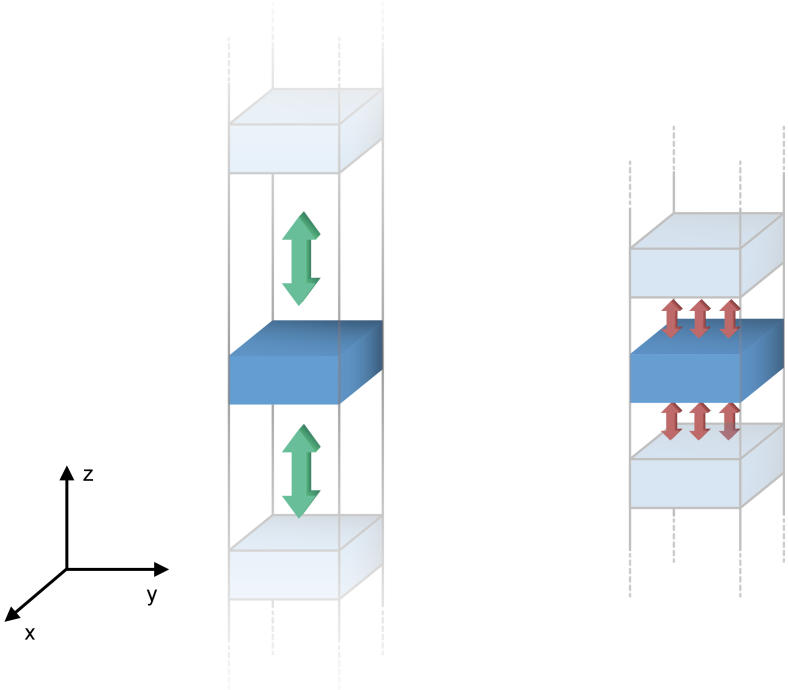

Figure 5.1: Influence of the vacuum height above and below the sample. On the left, green arrows represent a sufficient spacing between replicas on the z axis, whereas on the right the short distance between the sample and its periodic images lead to spurious interactions (red arrows).

volume of the box.

Choice of the cell dimensions

In order to obtain systems each containing an exact number of smectic layers, we adjusted the cell section accordingly to the following relation:

$$n_l = \frac{n_{mol} \cdot A_{mol}}{A_{cell}} \tag{5.1}$$

Here, n_l is the calculated number of layers as a function of the area of the horizontal cell section A_{cell}, n_{mol} is the number of molecules in the sample (in this case 1500) and A_{mol} is the area of the cell section occupied by each vertical 8CB molecule. It can be seen from Equation 5.1 that the number of layers is inversely proportional to the cell section area. Therefore, increasing A_{cell} area results in a lower number of layers, whereas reducing it squeezes

the sample and leads to the formation of a higher number of layers. The critical step of this approach is the determination of A_{mol}, which can be found only by a trial and error procedure.

We decided to create cells with a squared base, i.e. the x and y cell side vectors have the same value. The starting system, which we obtained from the duplication of the bulk sample, was accomodated in a 64x64 Å^2 cell. After about 10 ns of simulation, the onset of approximately 6 layers was observed. In order to determine if a 64 Å cell side was the best one to contain 6 layers, we also run simulations in which the cell side vectors were set at 65, 63, 62 and 61 Å respectively. The reduction of the cell section area was obtained by increasing the system pressure whilst the expansion was performed by manually setting cell vectors.

We then compared the density distributions $g(z)$ along the layer normal of the sample in each cell and concluded that the one with 62 Å sides, corresponding to a section area of 38.4 nm^2, was the one that accomodated the 6 layers at best, given that it featured the sharpest and most regular $g(z)$ peaks. From Equation 5.1 we derive that for a cell with a section of 38.4 nm^2 the average value of A_{mol} is 15.4 Å^2. This value was then employed to obtain an estimate of the x and y cell sides at which the smectic sample possesses a desired number of layers n_l (see Figure 5.2).

Once the appropriate cell dimensions were determined, we ran a series of NVT simulations at T=300 K for systems possessing a $n_l = 1 - 6$, including also those which should feature a half integer value of n_l (see Figure 5.3 for a snapshot of samples studied herein). It must be told in advance that samples with a half integer value of n_l never gave rise to the formation of half bilayers, instead the formation of an additional, lower density bilayer was found. Each simulation was run for at least 100 ns of production time.

In order to observe the influence of the free surface on the transition temperatures, we also run a serie of NVT simulations at temperatures ranging from 310 to 325 K for the sample possessing 6 layers for at least 50 ns of production time.

The conditions under which we studied smectic films were the same employed for the bulk system, exception made for the pressure barostat, which

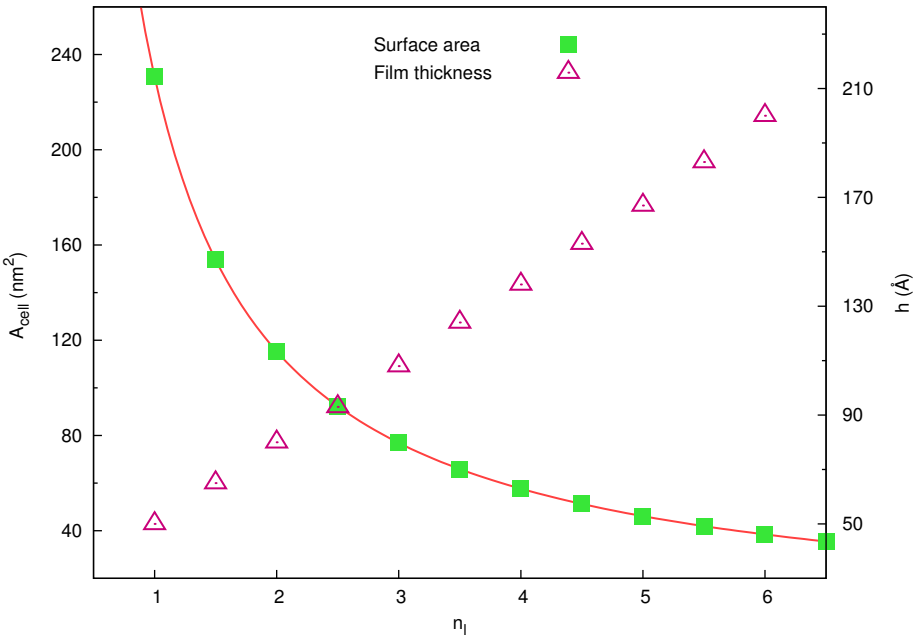

Figure 5.2: Horizontal cell section area A_{cell} and film thickness h as a function of the calculated number of layers n_l for the studied systems.

was turned off in order to simulate a vacuum environment and to keep the box shape and volume constant.

5.3 Study of 8CB thin film at different thickness

5.3.1 Surface tension

General definition

At constant temperature and pressure, the surface tension can ben defined as the derivative of the Gibbs free energy with respect to the surface area:

$$\gamma = \left(\frac{\partial G}{\partial A}\right)_{T,P,n} \tag{5.2}$$

In the bulk of a liquid, each molecule is equally attracted by its neighbours,

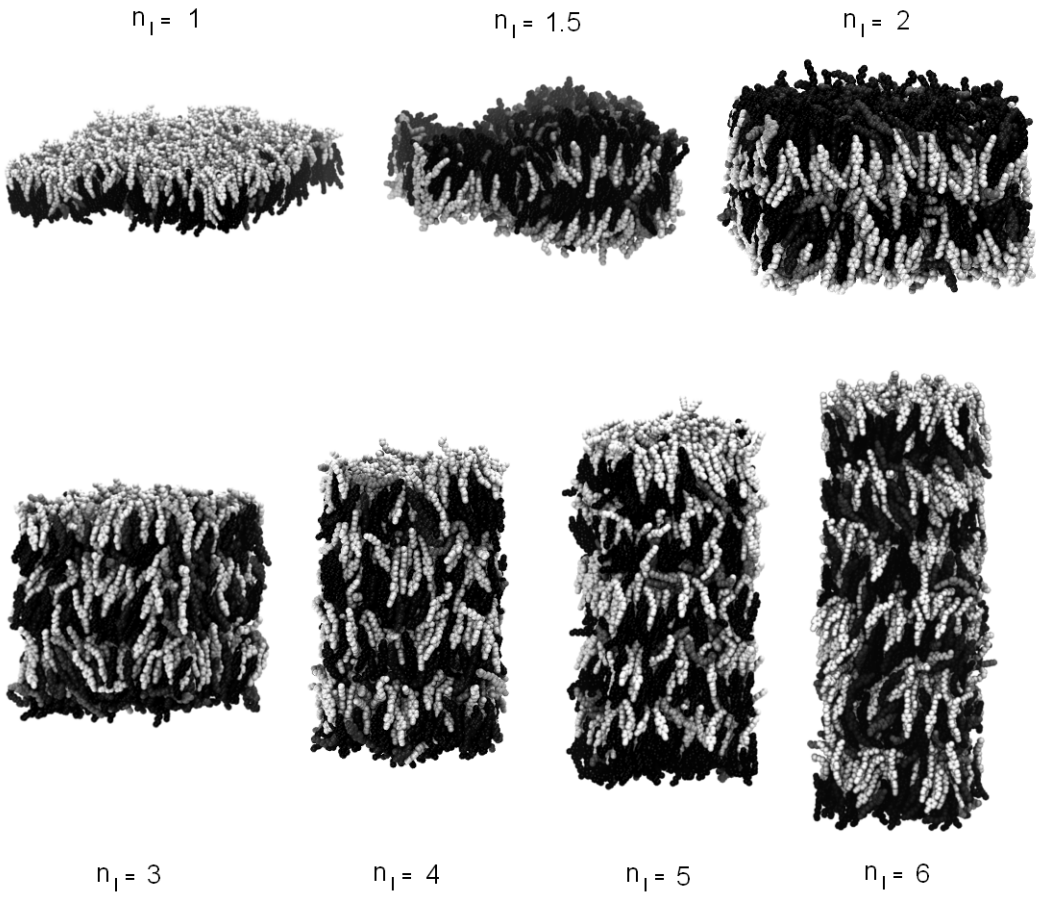

Figure 5.3: Equilibrated configurations of films with different thickness studied in this thesis.

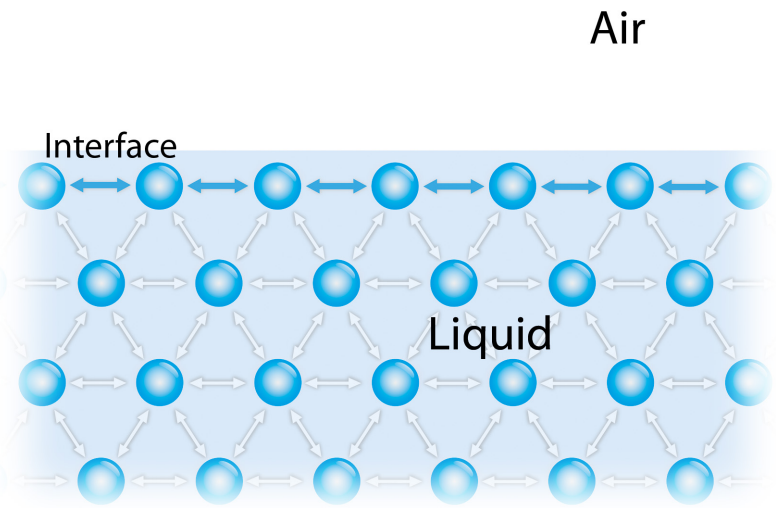

Figure 5.4: Graphical representation of the surface tension at the liquid-air interface. Arrows represent the intermolecular forces acting between the particles of the fluid.

resulting in a strong cohesive force. Conversely, molecules lying on the surface experience an imbalance of forces that usually results in the molecules being pulled toward the rest of the liquid (see Figure 5.4). Surface tension has the dimension of force per unit length, e.g. dyn/cm. Alternatively, this property is often expressed in terms of energy per unit area e.g. erg/cm^2. In this case we will talk about surface energy, which is defined as the energy difference between the bulk sample and one with any surface exposed to a different phase. Knowledge about surface tension and the mechanisms underlying its origin is critical in addressing such basic surface science phenomena such as wetting, adhesion, friction, spreading and detergency.

Surface tension of simulated thin films

Obtaining an estimate of the surface tension from simulations is fairly straightforward since the average value of the potential energy for every system is known.

Surface energy can be calculated as the difference between the average potential energy of each film U_{film} and the one of the bulk U_{bulk}, the latter

corresponding to 3.69·10^{-14} mJ. Neglecting entropic effects, the ratio between such excess energy and twice the surface area of each film (since each sample has two interfaces with the vacuum) returns the surface tension:

$$\gamma = \frac{U_{film} - U_{bulk}}{2A_{cell}} \tag{5.3}$$

In Table 5.1, the values of the potential energy for systems with different number of theoretical layer n_l is reported. The film featuring just one layer (n_l=1) has a higher value of potential energy compared to the other samples, even than those with half integer n_l (see also Figure 5.5), therefore suggesting that such system may be unstable. This is in agreement with the fact that the thinnest film which can be prepared experimentally is at least two layers thick[77].

Table 5.1: Calculated number of layers n_l , area of the horizontal cell section A_{cell}, potential energy of the film per molecule U_{film}, excess of potential energy with respect to the bulk sample due to the presence of two surfaces U_{surf} and the surface tension γ.

n_l	$A(10^{17}m^2)$	$U_{film}(10^{14}mJ)$	$U_{surf}(10^{18}mJ)$	$\gamma(mN/m)$
1	23.1	3.763	7.43	24.1
1.5	15.4	3.741	5.18	25.3
2	11.4	3.720	3.09	20.3
2.5	9.22	3.727	3.82	31.1
3	7.74	3.710	2.10	20.3
3.5	6.56	3.716	2.68	30.7
4	5.78	3.704	1.48	19.2
4.5	5.13	3.708	1.95	28.6
5	4.62	3.702	1.28	20.7
5.5	4.23	3.704	1.48	26.3
6	3.84	3.699	0.98	19.2

In Figure 5.5 the potential energy of the sample is plotted as a function of n_l. It can be seen that the potential energy of the system decreases as the number of layers increases. This is because the more layers are added, the less significant the fraction of molecules on the surface becomes compared

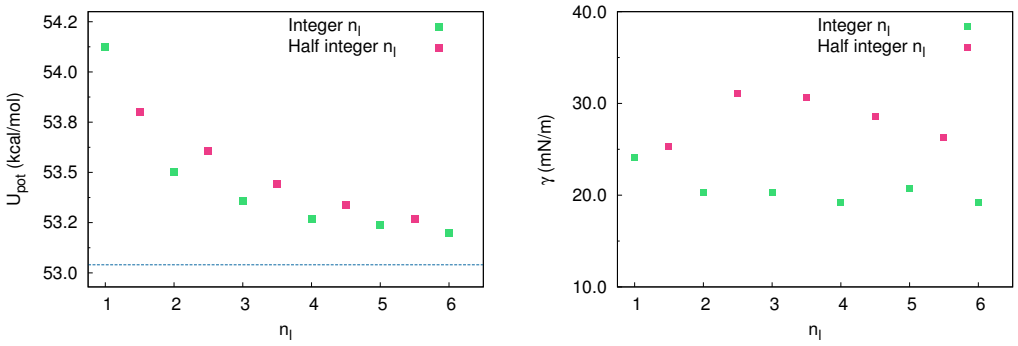

Figure 5.5: On the left, potential energy U_{pot} per mole as a function of n_l. The dashed blue line represents the value of energy for the bulk system. On the right, surface tension γ as a function of n_l.

to the total number of molecules. It can be assumed that for systems with a high n_l, the potential energy will tend to the one of a bulk sample. It can also be seen that simulated samples possessing a half integer value of n_l show a higher value of potential energy, indicating that they are less stable than the ones with integer n_l. It is worth noting that as the half integer n_l increases, the stress on the smectic structure rising from the excess/lack of molecules needed to fit at best the horizontal cell section can be distributed more efficiently. Therefore, we can expect that for high n_l, the excess of energy in samples featuring a surface/volume ratio that does not correspond to a finite number of layers becomes always smaller and eventually negligible, as shown in Figure 5.5. It must be noted that experimentally it is not possible to draw stable films with non integer n_l because of the presence of the meniscus, which acts as a reservoir of molecules, thus behaving as a buffer for the excess/lack of molecules created when we try to arbitrary set the surface/volume ratio, i.e. extend or reduce the surface of the film in a continuous manner.

Still in Figure 5.5, the trend of the surface tension is reported for both samples with integer and half integer n_l. Experimental measures show that for very thin films (with n_l up to 100) the surface tension can be considered constant with respect to the thickness[78]. Instead, thick films show a linear increment of the tension with the number of layers due to the pressure

difference caused by the concave meniscus[78–80]. The surface tension of simulated systems with integer n_l shows a constant trend, with an average surface tension of 19.9 $\pm$ 0.7 mN/m, not far from experimental measurements, which range from 24 to 30.9 mN/m depending on the technique[81]. Samples featuring a half integer n_l possess a higher value of γ than those with integer n_l but, as mentioned above, we expect such difference to decrease as systems with a high n_l are progressively considered.

5.3.2 Positional order

The main purpose of this section is to inspect the influence of the two free surfaces on the positional order of the sample. Many liquid crystals are known to align homeotropically exposing their alkyl chains to a surface with air or vacuum[82] in order to minimize the portion of molecule exposed to the surface and the loss of attractive interactions with the neighbours. This peculiar behaviour originates from the anisotropy of the molecular shape, which for LCs like 8CB is elongated. The homeotropical disposition of molecules at the interface promotes the formation of layers oriented perpendicularly to the surface across the whole sample and also induces a high positional order near the surface.

As a consequence, the most outstanding feature of these systems is that they show considerably high oscillations in the density profile along the z axis of the cell. Differently from simulations of the bulk system, in this case the z axis of the cell corresponds also to the phase director, which is normal to the surface/layers.

As already discussed in the previous chapter, the positional order of a smectic phase can be expressed in terms of the smectic order parameter $\langle\tau\rangle$ (see Equation 4.6). By linear interpolation of density distributions $g(z)_{tot}$ for samples possesing an integer n_l with equation 4.6, we obtain an average $\langle\tau\rangle$ of 0.36, which is an order of magnitude greater than the one found for the bulk phase $\langle\tau_{bulk}\rangle \backsimeq 0.025$. This indicates a strong influence of the surface on the positional order in thin films.

Even though performing a linear interpolation can give us an approximate

estimate of the positional order in our systems, it is experimentally known that the effect of the surface is relevant only in its proximity. In particular, the positional order parameter assumes the highest value at the surface (τ_{surf}) and decays exponentially towards $\tau_c = \tau(z = 0)$ as we move away from the interface. The excess of smectic order parameter τ_{exc} as a function of the distance on the z axis from the surface can be defined as[80]:

$$\begin{aligned} \tau_{exc}(z) &= \tau(z) - \tau_c \\ &= \frac{\tau_{surf}}{\cosh\left(\dfrac{h}{\sqrt{2}\,\xi}\right)} \cosh\left(\frac{\sqrt{2}\,z}{\xi}\right) \end{aligned} \tag{5.4}$$

where ξ is the correlation length and h is the film thickness. The hyperbolic cosine term accounts for the exponential decays of the order moving away from the surface, given that $\cosh(z) = \frac{1}{2}(e^z + e^{-z})$. Unfortunately, it is difficult to compare the behaviour expected from a theoretical point of view with the results of our simulations due to the limited thickness h of the simulated samples. Nevertheless, we attempted to fit our density profiles combining the following simplified version of Equation 5.4

$$\tau_{exc}(z) = \alpha\tau_{surf} \cdot \cosh(\beta z) \tag{5.5}$$

with the function previously used to interpolate density profiles of the bulk sample in Chapter 4 (Equation 4.6) obtaining the following:

$$g(z) = 1 + (\tau_{exc}(z) + \tau_c)\cos qz \tag{5.6}$$

It must be noted that this simplified function describing the variation of τ features two independent parameters α and β, even though they are theoretically correlated since they both contain ξ. This was done because of the impossibility to perform a direct numerical evaluation of ξ since we run into

an integer overflow error when computing the value of the hyperbolic term at the denominator during the fit procedure.

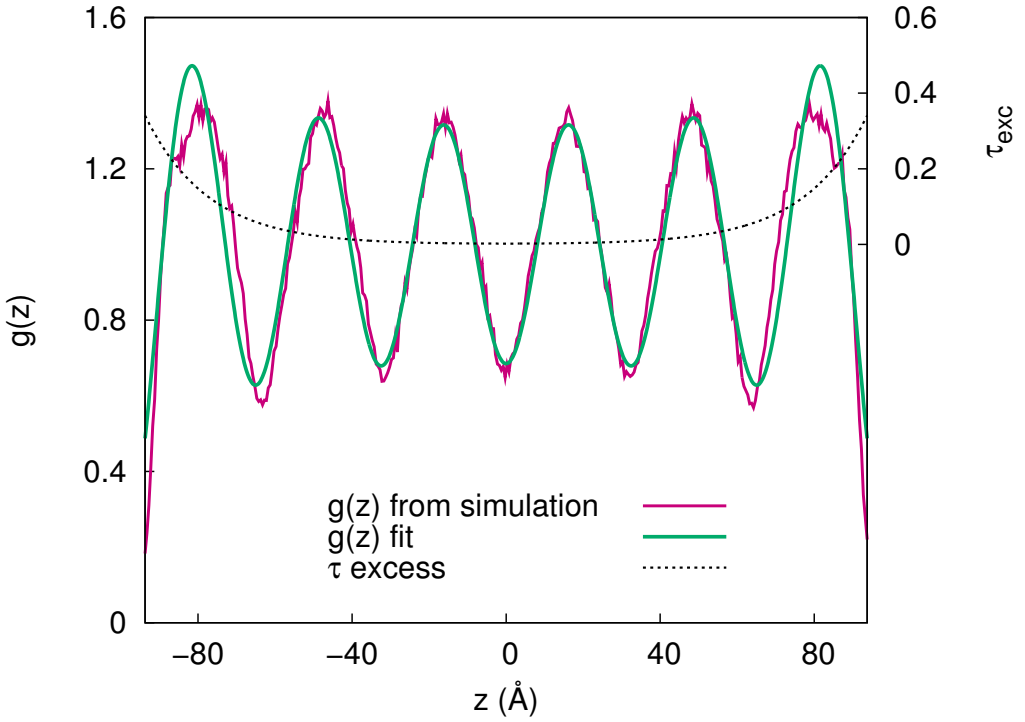

Figure 5.6: Fit of the normalized density profile along the z axis for the 6 layer film through Equation 5.5.

In Figure 5.6 we report the normalized density profile of a simulated film with n_l=6 together with the fit performed through Equation 5.6 and the trend of $\tau_{exc}(z)$. The fitting function reproduces with good precision the amplitude of $g(z)$ oscillations for the simulated film, particularly in the inner region of the sample, while the density oscillation at the surface and thus τ_s is slightly overstimated. Fit parameters are reported in Table 5.2 while in Figures 5.7 and 5.8 the density profile $g(z)_{tot}$ of the simulated films are shown.

Table 5.2: Calculated number of layers n_l - parameters derived from the fit: positional order parameter at the surface τ_s and in the middle of the film τ_c, correlation length ξ, fit parameter α, film thickness h' - film thickness from $g(z)$ density profiles h.

n_l	τ_s	τ_c	ξ (Å)	α	h' (Å)	h (Å)
2	0.47	0.43	12.4	47.1	71	80
3	0.46	0.39	15.8	70.2	103	108
4	0.46	0.37	17.8	117	130	138
5	0.46	0.35	18.5	188	160	167
6	0.47	0.31	18.8	334	181	200

It can be observed that for each film the density oscillation for the two external layers exposed directly to the vacuum is higher compared to the internal ones. This is confirmed by fitted data in Table 5.2, given that the value of τ_c is always smaller than τ_s. It is also evident that the value of τ_c decays as the number of layers increases, and is much higher than the one found for the bulk sample at the same temperature. This suggests that the influence of the surfaces is still relevant in the central region of the film. Nonetheless, it appears that τ_s is constant with the number of layers and thus does not depend on the film thickness h.

As already discussed in the previous chapter, 8CB layers are more appropriately referred to as bilayers, given that each of them is composed by two interdigitated layers of molecules oriented in the same direction. While for the bulk sample the density distributions for “up” and “down” sublayers are almost identical, apart from the phase shift, in the case of smectic films an asymmetry is induced by the two surfaces (see Figures 5.7 and 5.8). This is particularly evident for the two external bilayers, where the sublayer facing the vacuum has a considerably sharper density distribution compared to the one facing the bulk of the sample. Since each sublayer is composed by molecules oriented in the same direction and 8CB possesses a dipole moment μ of about 6 Debye in gas phase, then the two surfaces possess a non null opposite dipole moment given the higher density of the external sublayers.

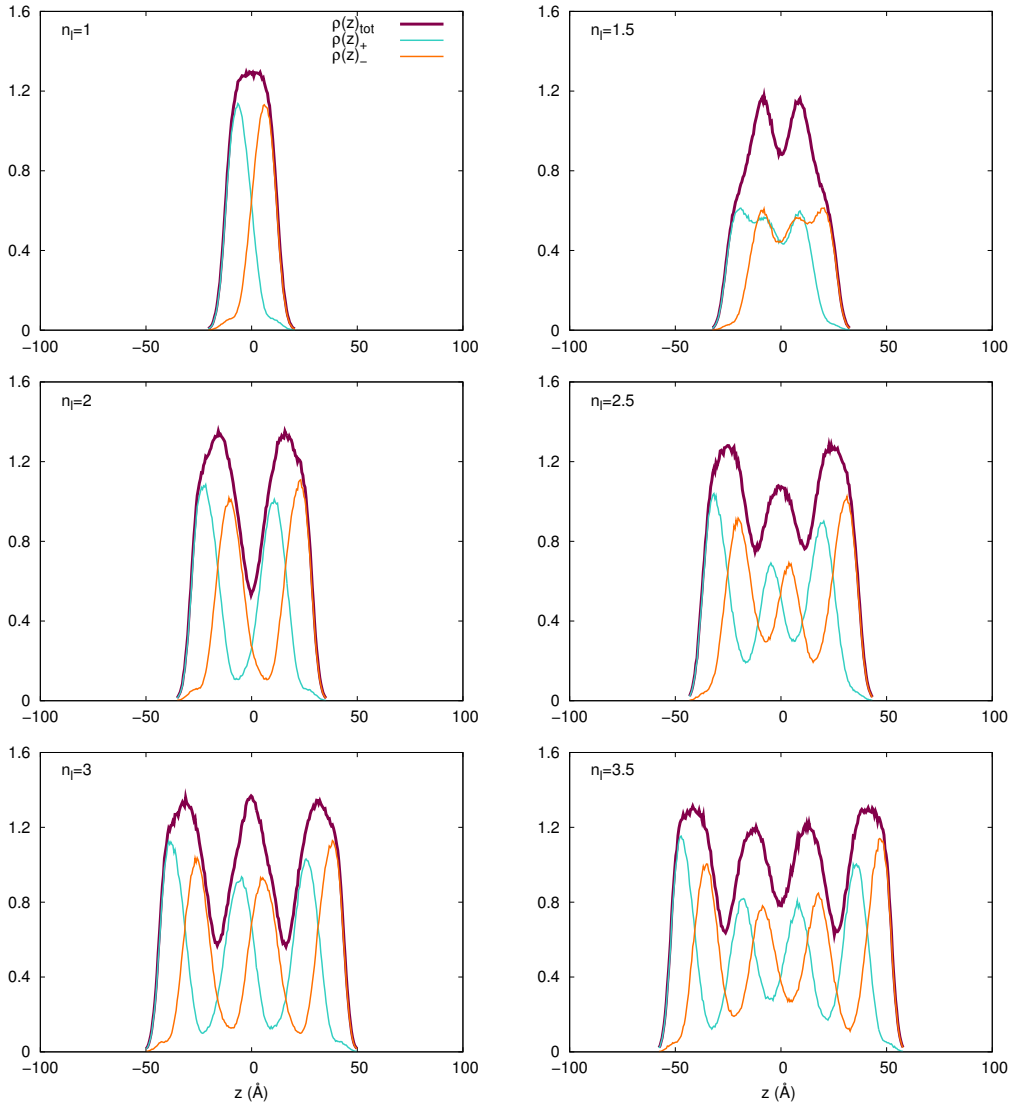

Figure 5.7: Density profiles along the z axis for samples with n_l =1, 1.5, 2, 2.5, 3, 3.5.

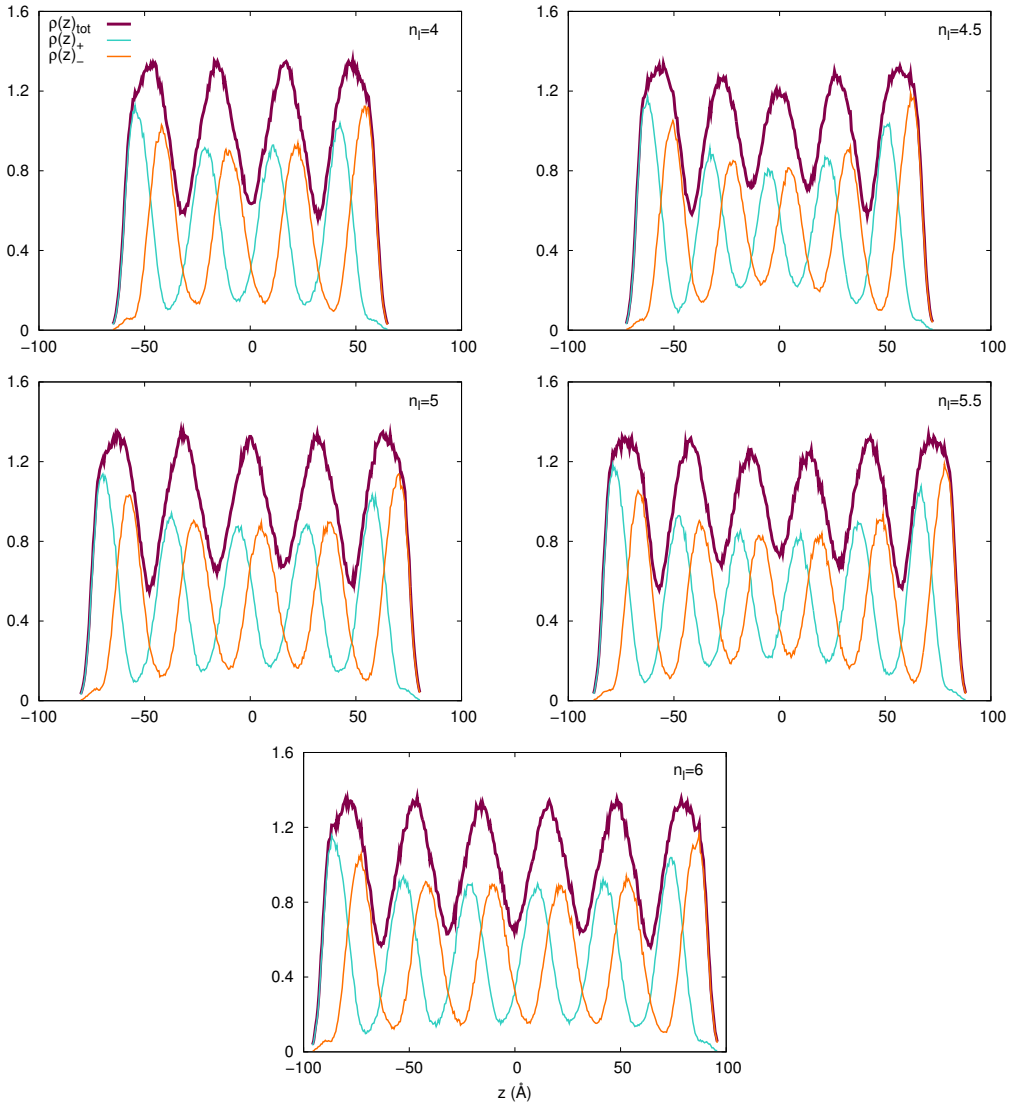

Figure 5.8: Density profiles along the z axis for samples with n_l =4, 4.5, 5, 5.5, 6.

5.3.3 Pressure profiles along the normal to the layers

Lateral pressure profiles measurements are difficult to perform due to the absence of direct experimental techniques. Instead, computer simulations allow to study pressure profiles at the atomistic scale[83]. At each time step of the simulation, the istantaneous pressure is computed from both the kinetic and potential pairwise interactions, the latter including electrostatic and van der Waals contributions. The pressure tensor $\mathbf{P}$ can be computed as:

$$\mathbf{P} = \begin{bmatrix} P_{xx} & P_{xy} & P_{xz} \\ P_{yx} & P_{yy} & P_{yz} \\ P_{zx} & P_{zy} & P_{zz} \end{bmatrix} = \left[\sum_i m_i \mathbf{v}_i \otimes \mathbf{v}_i - \sum_{i<j} \mathbf{F}_{ij} \otimes \mathbf{r}_{ij} \right] / V \qquad (5.7)$$

where the first term, which includes the mass m_i and velocity $\mathbf{v}_i$ of the i-th particle, represents the kinetic contribution to the pressure, whereas the potential component is given by the virial term defined as the cross product between the force $\mathbf{F}_{ij}$ acting on two i, j particles separated by a distance $\mathbf{r}_{ij}$. While the off-diagonal elements of $\mathbf{P}$ vanish at the equilibrium, the diagonal ones are expected to be equal for isotropic systems and conversely are non equal for anisotropic systems. In particular, for a planar system like 8CB thin films, we expect the two elements P_{xx} and P_{yy} to be equal but to have a different value from P_{zz}. Pressure profiles were obtained by diving the cell along the z axis in slabs with a height of 2 Å and computing the local pressure in each slab as implemented in NAMD[48].

In Figure 5.9 we report the planar pressure $(P_{xx} + P_{yy})/2$, the normal pressure P_{zz}, the scalar average pressure $(P_{xx} + P_{yy} + P_{zz})/3$ and the difference between the normal and planar pressure $P_{zz} - (P_{xx} + P_{yy})/2$ computed in each slab. Negative pressure values indicate the presence of attractive forces and thus the tendency of a certain portion of the system to compress, while positive values of pressure correspond to repulsive forces which lead to expansion.

It can be seen that in correspondence of sublayers, molecules experience a compressive force on the plane, while the pressure along the normal to the

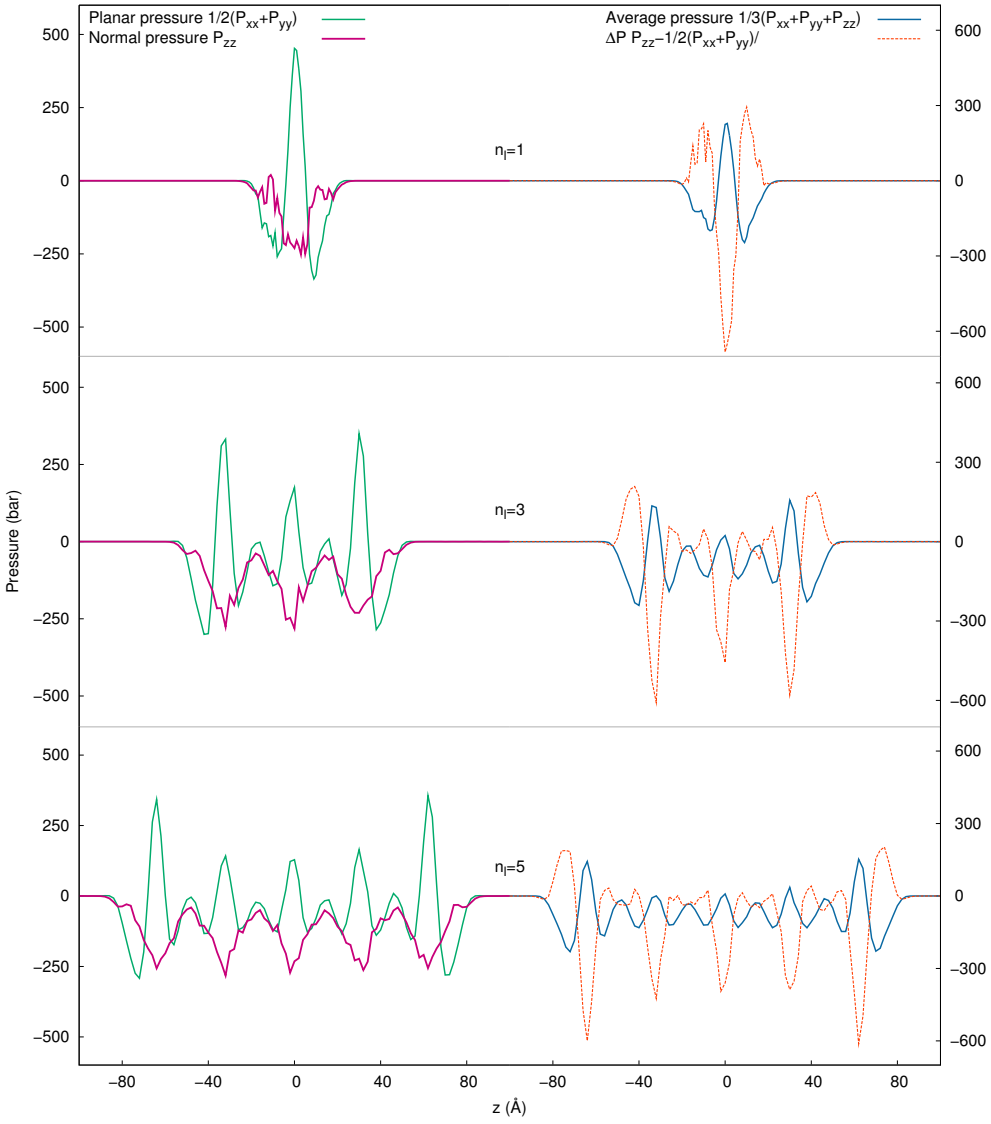

Figure 5.9: Pressure profiles along the z axis of the cell

layers, which is always negative across the whole sample, becomes relevant only at the internal edges of the sublayers. Moving to the interdigitation area, we notice that molecules repulse each other on the plane, exterting a positive pressure on the lateral faces of the cell slabs. At the same time, they experience a negative, compressive force along the layer normal and are therefore attracted to the interdigitation site. On the whole, the average pressure in the middle of two sublayers is always positive, suggesting that molecules will likely not diffuse through a bilayer. Instead, it becomes almost null or assumes slightly negative values between bilayers, indicating that molecules experience either a weak attractive force or no force at all, thus being free to diffuse from one side of a bilayer to another. The effect of the surface on the internal pressure can be noticed in particular on those samples featuring a higher number of layers, as it is evident that the highest positive and negative peaks are in proximity of the two interfaces and that their alternation is damped as we move toward the centre of the samples. The anisotropy of smectic films is also evident in the trend of the pressure difference ΔP, reflected by sharp negative and positive peaks, especially in proximity of the surface. The fluid can be considered isotropic only in the regions between bilayers, where the difference between the planar and normal pressure is close to zero.

5.3.4 Orientational order

In order to provide a quantitative measure of the degree of orientational order in 8CB films, we calculated the second rank order parameter $\langle P_2 \rangle$ using the same procedure reported in Chapter 4 for bulk samples. In Figure 5.10 we report the value of $\langle P_2 \rangle$ as a function of the number of layers.

We can say that for systems with an integer n_l, $\langle P_2 \rangle$ is on average constant and thus does not depend on the number of layers.

For samples featuring a half integer value of n_l, we can see an increasing trend of the order, with the exception of the system with n_l=1.5, which is characterized by the co-existence of two distinct regions featuring one and two layers respectively. Given that the majority of molecules belong to the

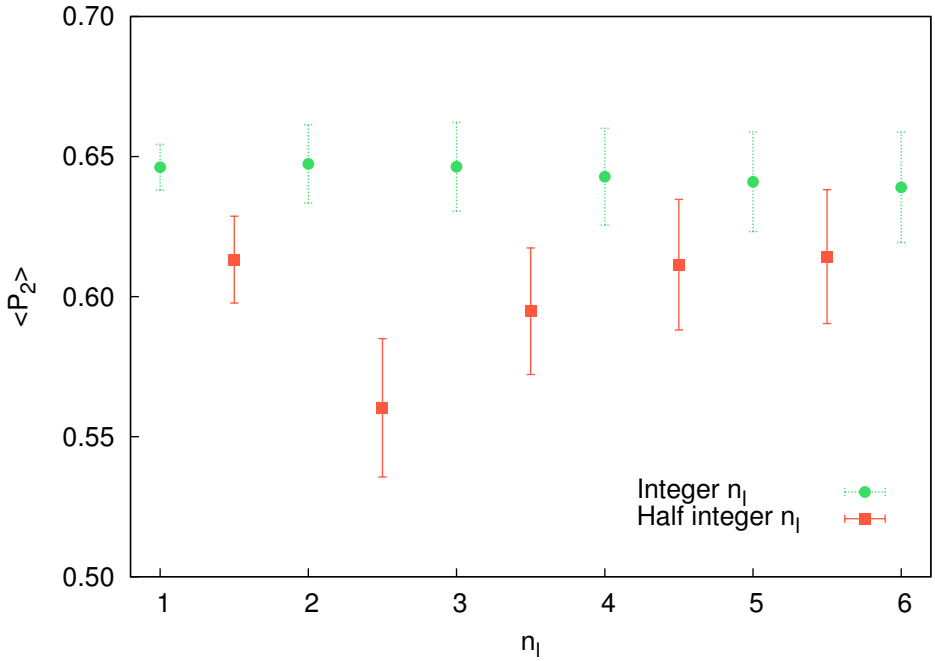

Figure 5.10: Second rank order parameter $\langle P_2 \rangle$ as a function of the number of layers.

region with two layers, we do not observe any major loss of orientational order of the sample, leading to quite high values of $\langle P_2 \rangle$. In the other samples featuring a half integer value of n_l, we do not observe the formation of distinct regions with different number of layers and the excess of molecules is dislocated on the whole sample. Therefore, $\langle P_2 \rangle$ raises with n_l as the space to fit the excess of molecules increases.

A thorough understanding of the orientational order in smectic thin films can be obtained by studying how the order parameter is related to the peculiar spatial organization of smectic bilayers. In Figure 5.11 the trend of the local $\langle P_2 \rangle$ as a function of the distance along the layer normal is reported. It can be seen that in general, for both samples with integer and half integer n_l, each peak is located in correspondence of a bilayer. The highest values of order parameter can be found at the very heart of each layer, while at its edges we observe a steep decreasing of the order parameter, probably caused by the presence of non aligned molecules at the layer boundaries. A slight excess of $\langle P_2 \rangle$ can be found at the interfaces, whereas peaks within

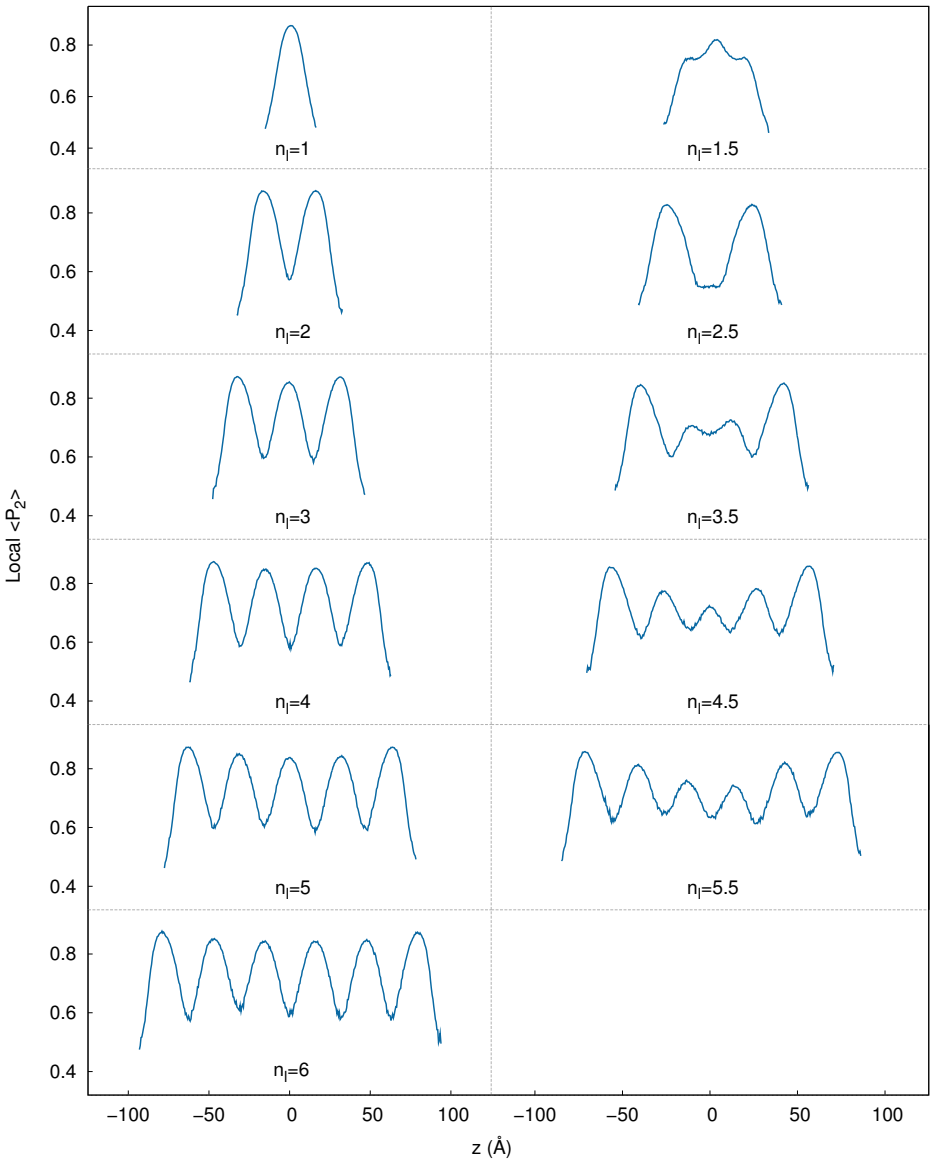

Figure 5.11: Second rank order parameter $\langle P_2 \rangle$ as a function of the distance along the layer normal.

the sample are slightly lower. For integer values of n_l, no dependence of the peak height as a function of n_l is observed; this explains the constant trend shown previously in Figure 5.10. Samples with half integer n_l feature lower peaks at the internal layers or no peaks at all for the case of n_l=2.5 layers (Figure 5.11). As the sample thickness increases, the disorder created by the excess of molecules can be better distributed and thus we observe gradually higher valued internal peaks, justifying again the trend of the total order parameter reported in Figure 5.10.

5.4 Temperature dependence of the order in a 8CB thin film

5.4.1 Positional and orientational order

The presence of a surface, other than leading to a higher positional order and inducing a homeotropical alignment of layers, exerts a major influence also on the transition temperatures of the LC phase. Experiments show that for a certain temperature T it exists a maximum film thickness $N(T)$ above which the film thins spontaneously, whereas films thinner than N are stable. In other words, we observe a phenomena called thinning transition, consisting in successive spontaneous layer-by-layer disruptions towards either the nematic or isotropic phase as the film is heated, each occurring at a precise temperature. These transitions are first order since the film thickness decreases by successive jumps of one or more layers. Smectic films can also exist above the bulk smectic-nematic transition T_{SmN}, forming a metastable system called presmectic film. Films above the T_{SmN} mantain the lamellar structure typical of smectic films, but the amplitude of density oscillations along the layer normal is much larger at the surface than in the center of the film. Thus, layers are much more defined at the surface than in the centre of the system. This effect becomes more and more prominent as the sample is heated and eventually leads to thinning transitions. It must be noted that in the case of 8CB, thinning temperatures cannot be determined for

systems composed by less than ten layers. This is due to the fact that the thinning temperature exceeds the nematic-isotropic liquid transition temperature, thus the meniscus melts and droplets of isotropic liquid slip into the film, which finally breaks[78].

In order to verify whether our model system is able to reproduce any of the previous experimental observations, we ran a series of simulations on the sample at n_l=6 by heating it from 310 to 325 K.

In Figure 5.12 we report the corresponding density profile along the layer normal $g(z)$ as a function of temperature. From now on, pairs of layers will be numbered progressively from $l = 1$ for the innermost ones to $l = n_l/2$ if n_l is even, or $l = (n_l - 1)/2$ if it is odd, with the central layer, if present, being $l = 0$. Since the studied sample possess $n_l = 6$, then the inner pair of layer will be $l = 1$, the external one $l = 3$ and the one in between $l = 2$. It can be seen that as the sample is heated into the nematic temperature range (310-312.5 K), density oscillations decrease in its middle, while layers on the surfaces remain well defined, in agreement with experimental observations. The transition can be studied more in detail by observing the trend of $\langle\tau\rangle$ for each pair of layers in Figure 5.13. While the external layers ($l = 3$) experience only a slight loss of positional order as the temperature is increased, those with $l = 1, 2$ show a substantial decay of $\langle\tau\rangle$ between 311 and 315 K. For layers with $l = 1$ the order parameter lowers much more quickly than those with $l = 2$, even though we cannot safely state that the system undergoes a layer by layer thinning transition. It is worth noting that even after the transition between 312.4 and 314 K, the value of $\langle\tau\rangle_{l=2}$ is still comparable with the ones of the bulk sample studied in Chapter 4. Most of the previous observations hold also for the density profiles of sublayers, even though they feature a much larger variation of $\langle\tau\rangle$ with the distance along the z axis.

We have seen that due to the presence of the surface, 8CB thin films present a smectic phase in the temperature range corresponding to the nematic phase for the bulk sample. Moreover, we have noticed the presence of an order-disorder transition, located close to T_{NI}, which leads to the onset of a mesophase that does not feature any positional order, which could either be

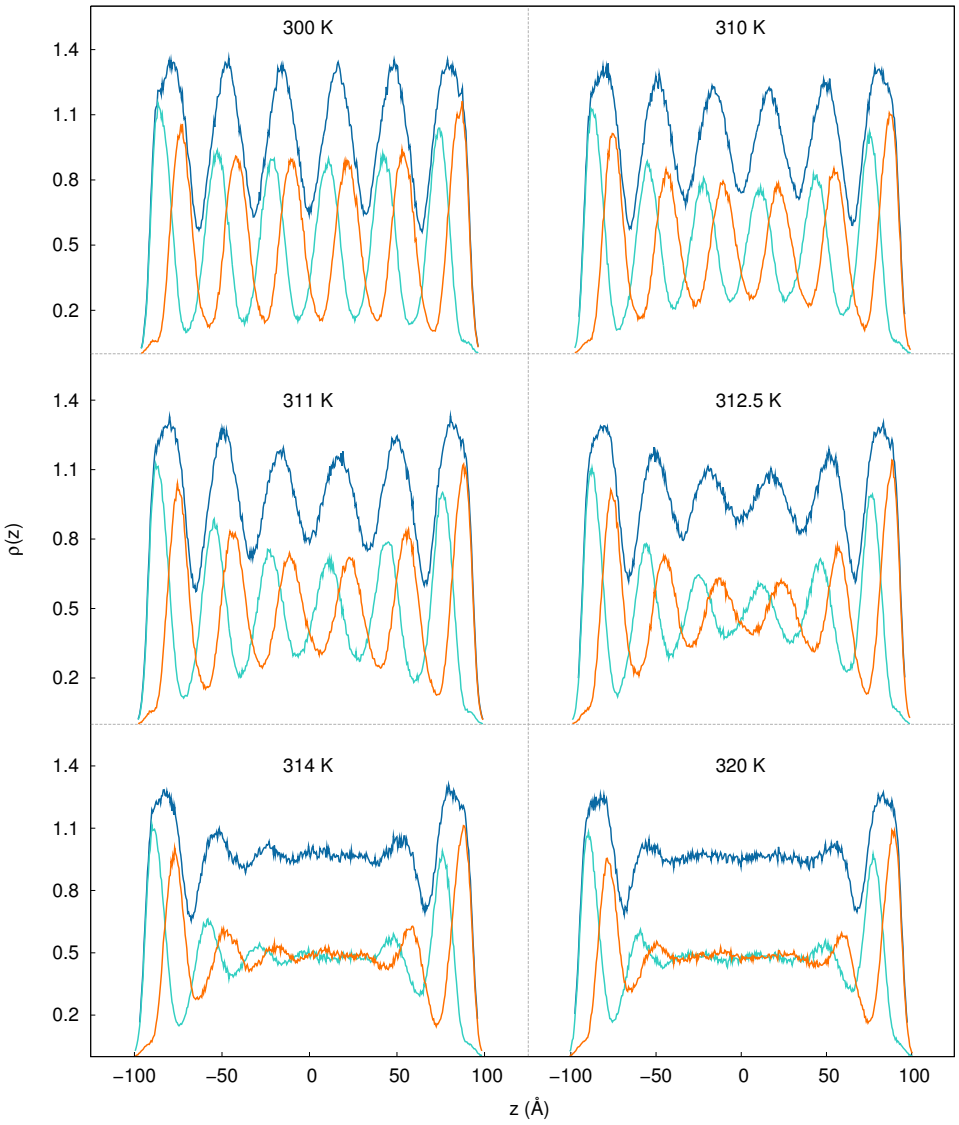

Figure 5.12: In blue line, the total density profiles along the z axis. Light blue and orange lines corresponds to the density profiles of up and down molecules.

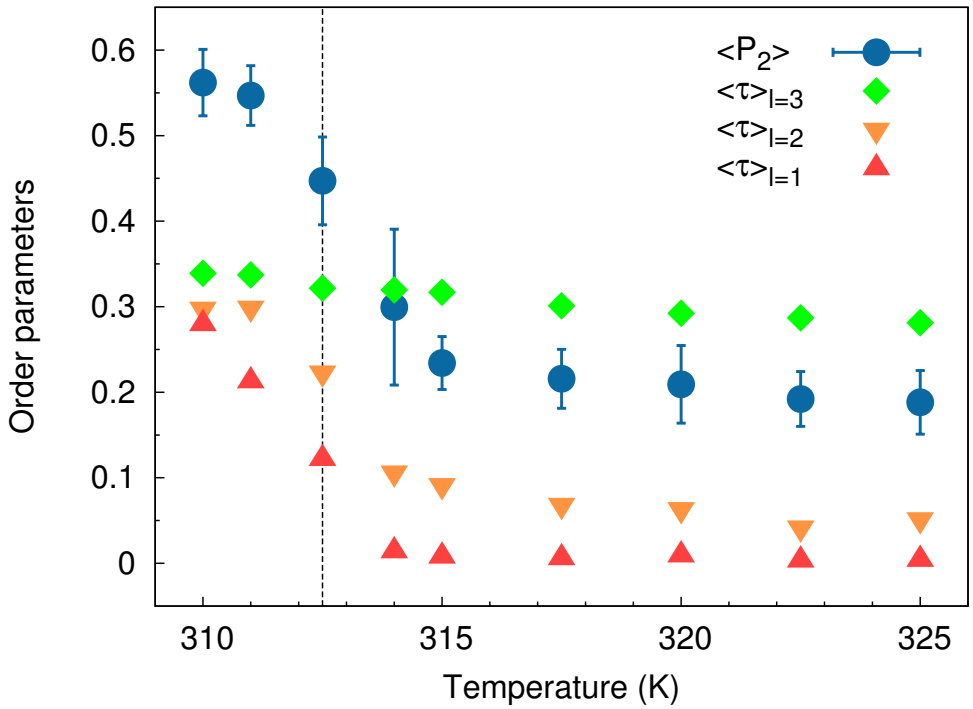

Figure 5.13: Second rank average order parameter $\langle P_2 \rangle$ and average positional order parameter $\langle \tau \rangle$ for layer pairs $l = 1, 2, 3$. The black vertical dashed line represents the T_{NI} of the bulk sample.

a nematic or isotropic phase.

In Figure 5.13 the trends of $\langle P_2 \rangle$ and $\langle \tau \rangle$ as a function of the temperature are reported. Before T_{NI} the system possesses high values of both orientational and positional order parameter, indicating the presence of a smectic phase. After 313 K, $\langle P_2 \rangle$ drops to 0.2, suggesting the presence of a direct transition from a system with high orientational and positional order to an isotropic system. The simultaneous decline of the order indicates the loss of nematic phase for very thin films like the one studied in this work.

Figure 5.14 reports the variation of the orientational order as a function of the position in the film. Compared to the sample at 300 K, systems heated to the nematic temperature range feature smaller and less defined peaks of $\langle P_2 \rangle$ in correspondence of layers with $l = 1, 2$, while the order at the surface remains substantially unchanged even at high temperatures. As the system is brought over the T_{NI}, the orientational order profile in the

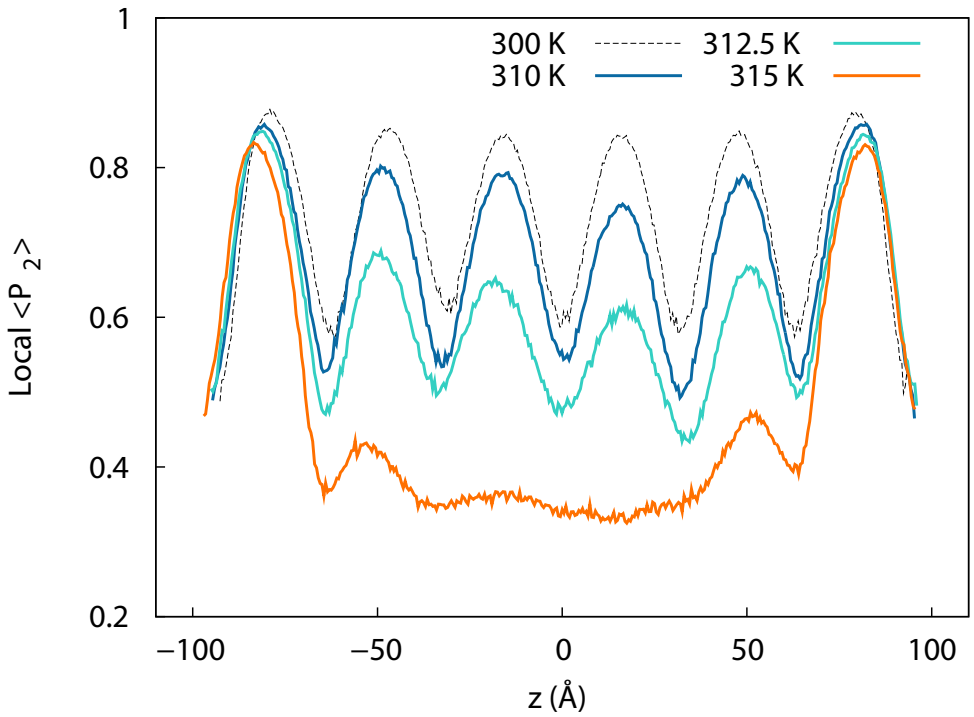

Figure 5.14: Second rank order parameter $\langle P_2 \rangle$ as a function of the distance along the layer normal and temperature for the sample with n_l=6.

inner portion of the sample becomes flat, exception made for the slight order excess present in layers with $l = 2$, revealed by the two small peaks just beside the interfaces.

5.5 Conclusions

The nature of low dimensional systems such as 8CB smectic thin films has been studied through atomistic Molecular Dynamics simulations. Several NVT simulations of a N=1500 molecules systems were run on films of various thickness and at different temperatures in order to study the influence of the interface on the orientational and positional order as well as on phase transitions. The surface tension of the system was found to be constant with respect to the number of layers and its value is comparable with experimental measurements. The influence of the surface on both the positional and orientational order was studied, obtaining a qualitative estimate of the excess of order and of its variation across the system, the latter being compared to the theoretical model proposed by Picano et al.[80] with good agreement. The dependence of the positional and orientational order with respect to the temperature was also studied, and the disappearance of the nematic phase was found for a thin film 6 layers thick.

Bibliography

[1] B. J. Alder and T. E. Wainwright. Phase transition for a hard sphere system. *J. Chem. Phys.*, 27:1208, 1957.

[2] B. J. Alder and T. E. Wainwright. Studies in molecular dynamics. i. general method. *J. Chem. Phys.*, 31:459, 1959.

[3] J. B. Gibson, A. N. Goland, M. Milgram, and G. H. Vineyard. Dynamics of radiation damage. *Phys. Rev.*, 120:1229, 1960.

[4] A. Rahman. Correlations in the motion of atoms in liquid argon. *Phys. Rev.*, 136:405, 1964.

[5] L. Verlet. Computer "experiments" on classical fluids. i. thermodynamical properties of lennard-jones molecules. *Phys. Rev.*, 159:98–103, 1967.

[6] L. Verlet. Computer "experiments" on classical fluids. ii. equilibrium correlation functions. *Phys. Rev.*, 165:201, 1967.

[7] J. P. Hansen and L. Verlet. Phase transitions of the lennard-jones system. *Phys. Rev.*, 184:151, 1969.

[8] A. Rahman and F. H. Stillinger. Improved simulation of liquid water by molecular dynamics. *J. Chem. Phys.*, 60:1545, 1974.

[9] J. A. McCammon, B. R. Gelin, and M. Karplus. Dynamics of folded proteins. *Nature*, 267:585, 1977.

[10] R. Car and M. Parrinello. Unified approach for molecular dynamics and density-functional theory. *Phys. Rev. Lett.*, 55:2471, 1985.

[11] H. J. C. Berendsen, J. P. M. Postma, A. DiNola, and J. R. Haak. Molecular dynamics with coupling to an external bath. *J. Chem. Phys.*, 81:3684, 1984.

[12] D. Fincham and D. M. Heyes. Recent advances in moleculardynamics computer simulation. *Adv. in Chemical Physics*, 63:493–575, 1985.

[13] D. Frenkel and B. Smit. *Understanding Molecular Simulations: From Algorithms to Applications*. Academic Press, San Diego, 1996.

[14] E. Paci and M. Marchi. Taming the ewald sum in molecular dynamics simulations of solvated proteins via a multiple time step algorithm. *J. Phys. Chem*, 104:3003, 1996.

[15] M. Parrinello and A. Rahman. Polymorphic transitions in single crystals: A new molecular dynamics method. *J.App.Phys.*, 52:7182–7190, 1981.

[16] M. P. Allen and D. J. Tildesley. *Computer Simulation of Liquids*. Oxford University Press, Walton Street, Oxford OX2 6DP, 1989.

[17] Polygen Corp. Parameter and topology files for charmm, version 22, Copyright 1986, Release 1992.

[18] W. F. van Gunsteren and H. J. C. Berendsen. *Groningen Molecular Simulation (GROMOS) Library Manual*. Biomos, Groningen, 1987.

[19] J. Wang, P. Cieplak, and P. A. Kollman. How well does a restrained electrostatic potential (resp) model perform in calculating conformational energies of organic and biological molecules? *J. Comput. Chem.*, 21:1049, 2000.

[20] W. L. Jorgensen and N. A. McDonald. Development of an all-atom force field for heterocycles. properties of liquid pyridine and diazenes. *Theochem - J. Molec. Structure*, 424:145, 1998.

[21] A. K. Rappè, C. J. Casewit, K. S. Colwell, W. A. Goddard, and W. M. Skiff. Uff, a full periodic table force field for molecular mechanics and

molecular dynamics simulations. *Journal of the American Chemical Society*, 114:10024–10035, 1992.

[22] N. L. Allinger, Y. H. Yuh, and J. Lii. Molecular mechanics. the mm3 force field for hydrocarbons. 1. *J. Am. Chem. Soc.*, 111:8551, 1989.

[23] S. K. Nath and R. Khare. New forcefield parameters for branched hydrocarbons. *J. Chem. Phys.*, 115:10837, 2001.

[24] H. Sunj. Compass: an ab initio force field optimized for condensed-phase applications overview with details on alkane and benzene compounds. *J. Phys. Chem. B.*, 102:7338–7364, 1998.

[25] A. C. T. van Duin, S. Dasgupta, F. Lorant, and W. A. Goddard III. Reaxff: A reactive force field for hydrocarbons. *J. Phys. Chem. A*, 105:9396, 2001.

[26] A. D. Mackerell. Empirical force fields for biological macromolecules: Overview and issues. *J. Comput. Chem.*, 25:1584–1604, 2004.

[27] Pitzer. *Disc. Faraday Soc.*, 107:4519–4529, 1951.

[28] P. Cieplak, W. D. Cornell, C. Bayly, and P. A. Kollmann. Application of the multimolecule and multiconformational resp methodology to biopolymers: Charge derivation for dna, rna, and proteins. *J. Comput. Chem.*, 16:1357–1377, 1995.

[29] R. Berardi, L. Muccioli, and C. Zannoni. Can nematic transitions be predicted by atomistic simulations? A computational study of the odd–even effect. *ChemPhysChem*, 5:104–111, 2004.

[30] Y. Olivier, L. Muccioli, V. Lemaur, Y. H. Geerts, C. Zannoni, and J. Cornil. Theoretical characterization of the structural and hole transport dynamics in liquid-crystalline phthalocyanine stacks. *J. Phys. Chem.B*, 13:14102–14111, 2009.

[31] T. A. Papadopoulos, L. Muccioli, S. Athanasopoulos, A. B. Walker, C. Zannoni, and D. Beljonne. Does supramolecular ordering influence

exciton transport in conjugated systems? insight from atomistic simulations. *Chemical Science*, 2:1025–1032, 2011.

[32] A. Pizzirusso, M. Savini, L. Muccioli, and C. Zannoni. An atomistic simulation of the liquid-crystalline phases of sexithiophene. *J. Mater. Chem.*, 21:125–133, 2011.

[33] I. Cacelli, C. F. Lami, and G. Prampolini. Force-field modeling through quantum mechanical calculations: Molecular dynamics simulations of a nematogenic molecule in its condensed phases. *J. Comput. Chem.*, 30:366–378, 2009.

[34] J. Peláez and M. R. Wilson. Atomistic simulations of a thermotropic biaxial liquid crystal. *Phys. Rev. Lett.*, 97:267801, 2006.

[35] C. Zannoni. Molecular design and computer simulations of novel mesophases. *J. Mater. Chem.*, 11:2637–2646, 2001.

[36] M. R. Wilson. Molecular simulation of liquid crystals: progress towards a better understanding of bulk structure and the prediction of material properties. *Chem. Soc. Rev.*, 36:1881–1888, 2007.

[37] I. Cacelli, L. De Gaetani, G. Prampolini, and A. Tani. Liquid crystal properties of the *n*-alkyl-cyanobiphenyl series from atomistic simulations with *ab initio* derived force fields. *J. Phys. Chem. B*, 111:2130–2137, 2007.

[38] S. J. Picken. Measurements and values for selected order parameters. In D. A. Dunmur, A. Fukuda, and G. R. Luckhurst, editors, *Physical Properties of Liquid Crystals, Vol. 1: Nematics*, chapter 2.2, pages 89–102. IEE, London, 2001.

[39] A. Sanchez-Castillo, M. A. Osipov, and F. Giesselmann. Orientational order parameters in liquid crystals: A comparative study of x-ray diffraction and polarized raman spectroscopy results. *Phys. Rev. E*, 81:021707, 2010.

[40] Y. Lansac, M. A. Glaser, and N. A. Clark. Microscopic structure and dynamics of a partial bilayer smectic liquid crystal. *Phys. Rev. E*, 64:051703, 2001.

[41] A. J. McDonald and S. Hanna. Atomistic simulation of a model liquid crystal. *J. Chem. Phys.*, 124:164906, 2006.

[42] L. De Gaetani and G. Prampolini. Computational study through atomistic potentials of a partial bilayer liquid crystal: structure and dynamics. *Soft Matter*, 5:3517–3526, 2009.

[43] M. J. Cook and M. R. Wilson. Simulation studies of dipole correlation in the isotropic liquid phase. *Liq. Cryst.*, 27:1573–1583, 2000.

[44] W. D. Cornell, P. Cieplak, C. I. Bayly, I. R. Gould, K. M. Merz, D. M. Ferguson, D. C. Spellmeyer, T. Fox, J. W. Caldwell, and P. A. Kollman. A second generation force field for the simulation of proteins, nucleic acids, and organic molecules. *J. Am. Chem. Soc.*, 117:5179, 1995.

[45] J. Wang, P. Cieplak, and P. A. Kollman. How well does a restrained electrostatic potential (resp) model perform in calculating conformational energies of organic and biological molecules. *J. Comput. Chem.*, 21:1049, 2000.

[46] G. Tiberio, L. Muccioli, R. Berardi, and C. Zannoni. Realistic transition temperatures and physical properties for n-cyanobiphenyls via molecular dynamics simulations. *ChemPhysChem*, 10:125, 2009.

[47] J. Peláez and M. R. Wilson. Molecular orientational and dipolar correlation in the liquid crystal mixture E7: a molecular dynamics simulation at a fully atomistic level. *Phys. Chem. Chem. Phys.*, 9:2968–2975, 2007.

[48] J. C. Phillips, R. Braun, W. Wang, J. Gumbart, E. Tajkhorshid, E. Villa, C. Chipot, R. D. Skeel, L. Kale, and K. Schulten. Scalable molecular dynamics with namd. *J. Comput. Chem.*, 26:1781, 2005.

[49] H. J. C. Berendsen, J. P. M. Postma, W. F. van Gunsteren, A. Di Nola, and J. R. Haak. Molecular dynamics with coupling to an external bath. *J. Chem. Phys.*, 81:3684–3690, 1984.

[50] U. Essmann, L. Perera, M. L. Berkowitz, T. A. Darden, H. Lee, and L. G. Pedersen. A smooth particle mesh Ewald method. *J. Chem. Phys.*, 103:8577–8593, 1995.

[51] A. Wuerflinger and M. Sandmann. Equations of state for nematics. In D. A. Dunmur, A. Fukuda, and G. R. Luckhurst, editors, *Physical Properties of Liquid Crystals, Vol. 1: Nematics*, chapter 3.3, page 151. IEE, London, 2001.

[52] D. A. Dunmur, A. Fukuda, and G. R. Luckhurst, editors. *Physical Properties of Liquid Crystals, Vol. 1: Nematics*, volume 25 of *EMIS Datareview Series*. IEE, London, 2001.

[53] R. G. Horn. Refractive indices and order parameters of two liquid crystals. *J. de Physique*, 39:105, 1978.

[54] I. Chirtoc, M. Chirtoc, C. Glorieux, and J. Thoen. Determination of the order parameter and its critical exponent for nCB ($n = 5 - 8$) liquid crystals from refractive index data. *Liq. Cryst.*, 31:229–240, 2004.

[55] H. F. Gleeson, C. D. Southern, P. D. Brimicombe, J. W. Goodby, and V. Görtz. Optical measurements of orientational order in uniaxial and biaxial nematic liquid crystals. *Liq. Cryst.*, 37:949–959, 2010.

[56] G. R. Luckhurst and G. W. Gray, editors. *The Molecular Physics of Liquid Crystals*. Academic Press, London, 1979.

[57] Y. Lansac, M. A. Glaser, and N. A. Clark. Microscopic structure and dynamics of a partial bilayer smectic liquid crystal. *Phys. Rev. E*, 64:051703, 2001.

[58] P. Pasini and C. Zannoni. *Advances in the Computer Simulations of Liquid Crystals*, pages 296–303. Kluwer Academic Publishers, 1998.

[59] T. Krentsel, O. Lavrentovich, and S. Kumar. In-situ x-ray measurements of light-controlled layer spacing in a smectic-a liquid crystal. *Mol. Cryst. Liq. Cryst.*, 304:463, 1997.

[60] R. G. Marguta, E. Martín del Río, and E. de Miguel. Revisiting mcmillan's theory of the smectic a phase. *J. Phys.: Condens. Matter*, 18:10335, 2006.

[61] W. L. McMillan. Simple molecular model for the smectic a phase of liquid crystals. *Phys. Rev. A*, 4:1238, 1971.

[62] M. Fukuto, O. Gang, K. J. Alvine, B. M. Ocko, and P. S. Pershan. Wetting of liquid-crystal surfaces and induced smectic layering at a nematic-liquid interface: An x-ray reflectivity study. *Phys. Rev. E*, 77:031607, 2008.

[63] Y. G. J. Lau, R. M. Richardson, and R. Cubitt. Smectic order induced at homeotropically aligned nematic surfaces: A neutron reflection study. *J. Chem. Phys.*, 124:234910, 2006.

[64] J. Zhang, J. Su, and H. Guo. An atomistic simulation for 4-cyano-4'-pentylbiphenyl and its homologue with a reoptimized force field. *J. Phys. Chem. B*, 115:2214–27, 2011.

[65] S. Urban, J. Przedmojski, and J. Czub. X-ray studies of the layer thickness in smectic phases. *Liq. Cryst.*, 32:619–624, 2005.

[66] S. V. Dvinskikh, I. Furó, H. Zimmermann, and A. Maliniak. Anisotropic self-diffusion in thermotropic liquid crystals studied by 1h and 2h pulse-field-gradient spin-echo nmr. *Phys. Rev. E*, 65:061701, 2002.

[67] K. S. Chu and D. S. Moroi. Self-diffusion in nematic liquid crystals. *J. Phys. Colloques*, 36:99–101, 1975.

[68] F. Volino and A. J. Dianoux. Application to self-diffusion in smectic phases. *Molec. Phys.*, 36:389, 1978.

[69] S. Miyajima, A. F. McDowell, and R. M. Cotts. Pulsed-field-gradient stimulated-spin-echo nmr study of anisotropic self-diffusion in smectic ad liquid crystal cbooa. *Chem. Phys. Lett.*, 212:277–282, 1993.

[70] G. J. Krüger, H. Spiesecke, and R. V. Steenwinkel. Nuclear magnetic relaxation and self diffusion in some liquid crystals showing smectic polymorphism. *J. Phys. Colloques*, 37:123–126, 1976.

[71] M. P. Lettinga and E. Grelet. Self-diffusion of rodlike viruses through smectic layers. *Phys. Rev. Lett.*, 99:197802, 2007.

[72] C. Y. Young, R. Pindak, N. A. Clark, and R. B. Meyer. Light-scattering study of two-dimensional molecular-orientation fluctuations in a freely suspended ferroelectric liquid-crystal film. *Phys. Rev. Lett.*, 40:773–776, Mar 1978.

[73] D. E. Moncton and R. Pindak. Long-range order in two- and three-dimensional smectic-b liquid-crystal films. *Phys. Rev. Lett.*, 43:701–704, Sep 1979.

[74] C. Rosenblatt, R. Pindak, N. A. Clark, and R. B. Meyer. Freely suspended ferroelectric liquid-crystal films: Absolute measurements of polarization, elastic constants, and viscosities. *Phys. Rev. Lett.*, 42:1220–1223, Apr 1979.

[75] H Dosch. *Critical Phenomena at Surface and Interfaces*. Springer Berlin, 1992.

[76] O. Gang, X. Z. Wu, B. M. Ocko, E. B. Sirota, and M. Deutsch. Surface freezing in chain molecules. ii. neat and hydrated alcohols. *Phys. Rev. E*, 58:6086–6100, Nov 1998.

[77] T. Stoebe, P. Mach, and C. C. Huang. Surface tension of free-standing liquid-crystal films. *Phys. Rev. E*, 49:R3587–R3590, May 1994.

[78] P. Oswald and P. Pawel. *Smectic and Columnar Liquid Crystals*, chapter VIII.2. Taylor & Francis Group, 2005.

[79] R. Jaquet and F. Schneider. Dependence of film tension on the thickness of smectic films. *Phys. Rev. E*, 67:021707, 2003.

[80] F. Picano, P. Oswald, and E. Kats. Disjoining pressure and thinning transitions in smectic-a liquid crystal films. *Phys. Rev. E*, 63:021705, 2001.

[81] F. Schneider. A novel method for measuring the surface tension of free standing smectic films. *Rev. Sci. Instrum.*, 73:114, 2002.

[82] B. D. Swanson, H. Stragier, D. J. Tweet, and L. B. Sorensen. Layer-by-layer surface freezing of freely suspended liquid-crystal films. *Phys. Rev. Lett.*, 62:909–912, Feb 1989.

[83] M. Patra. Lateral pressure profiles in cholesterol-dppc bilayers. *European Biophysics Journal*, 35:79–88, 2005.